CHALMERS
UNIVERSITY OF TECHNOLOGY

University of Stuttgart
Germany

Microstructure of Z-phase strengthened martensitic steels:

Meeting the 650°C challenge

Master's Thesis in Materials Engineering

ROBERT LAWITZKI

MASTERTHESIS

Microstructure of Z-phase strengthened martensitic steels:

Meeting the 650°C challenge

ROBERT LAWITZKI

Department of Physics
CHALMERS UNIVERSITY OF TECHNOLOGY
Gothenburg, Sweden
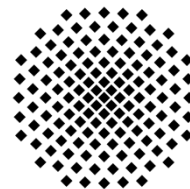
Institute of Materials Science
UNIVERSITY OF STUTTGART
Stuttgart, Germany

Diploma work in the Master programme Materials Engineering

Performed at: Chalmers University of Technology
SE – 412 96 Gothenburg
Sweden

Examiners: Assitant Prof. Dr. Fang Liu, Chalmers University of Technology
Prof. Dr. Dr. h.c. Guido Schmitz, University of Stuttgart

Microstructure of Z-phase strengthened martensitic steels:

Meeting the 650°C challenge

ROBERT LAWITZKI

Cover:

SEM secondary electron image of a 12 wt% Cr steel after electropolishing; reconstruction of an APT data set showing a volume on the tip of a specimen, which contains several precipitates; and a 1D concentration profile along the blue cylinder shown in the reconstruction.

Microstructure of Z-phase strengthened martensitic steels: Meeting the 650 °C challenge

Robert Lawitzki
Department of Physics
Chalmers University of Technology

Abstract

This work aids the development of a new generation of martensitic steels that enable working conditions of 650 °C / 350 bar. A new concept called *Z-phase strengthening* is applied, where the thermodynamically most stable phase in these steels, Z-phase, is used as the strengthening agent. These steels have a great potential to increase the thermal efficiency of fossil fired steam power plants, decrease their CO_2 emissions, and enhance their operational flexibility to better accommodate energy generation from renewable sources.

The microstructure of two Z-phase strengthened 9-12% Cr trial steels was studied. These two trial steel were designed to study three important issues: i) the effects of Mo addition on Laves-phase formation; ii) the effects of combining Nb and Ta on the Z-phase formation; iii) the effects of C content on the Z-phase formation.

Scanning electron microscopy was used to follow the evolution of Laves phase particle size, area fraction and number density in the these trial steels during aging at 600 °C, 650 °C, and 700 °C for up to 31 days. Compared with equilibrium calculations obtained by JMatPro and ThermoCalc, it is shown that Laves phase has almost fully precipitated after 31 days of aging at 650 °C and 700 °C, but not for aging at 600 °C. These results were verified by matrix investigations using atom probe tomography. Furthermore, atom probe tomography was used to investigate the evolution of the chemical compositions of carbonitrides and Z-phase during aging. The results show that Z-phase forms faster in carbonitrides with high nitrogen to carbon, and niobium to tantalum ratios.

Keywords: Z-phase, Laves phase, 9-12% Cr steels, precipitation strengthening, APT, SEM

Contents

List of Figures

List of Tables

List of Abbreviations

APT	Atom Probe Tomography
BSE	Backscattered Electrons
EDX	Energy Dispersive X-ray Spectroscopy
FEG	Field Emission Gun
FIB	Focused Ion Beam
QBSD	Four-Quadrant Backscattered Electron Detector
LEAP	Local Electrode Atom Probe
SE	Secondary Electrons
SEM	Scanning Electron Microscope
ToF	Time of Flight
VIM	Vacuum Induction Melting

1   Introduction

1.1   The 650 °C challenge

The rise of CO_2 concentration in the atmosphere is a worldwide problem, since CO_2 is a greenhouse gas and has a vital influence on the regulation of the earth's temperature. Fossil fired steam power plants are one of the biggest CO_2 emitters. Thus, one solution is to reduce their CO_2 emission. This is possible by increasing the power plants' energy conversion efficiency, which can be achieved by raising the pressure and temperature of the steam. The efficiency of fossil fired power plants is directly connected to the temperature of the steam. Theoretically, the maximum efficiency η of a thermodynamic engine is given by the Carnot cycle:

$$\eta = 1 - \frac{T_C}{T_H},$$
[1]

where T_C is the absolute temperature of the cold reservoir and T_H the absolute temperature of the hot steam. Practically, the Carnot efficiency cannot be reached and the Rankine cycle is used instead.

An increase in thermal efficiency can also decrease the fuel consumption of power plants. Therefore, there has always been an interest in raising the working temperatures and pressures of these power plants. Figure 1.1 shows the change in operation conditions of fossil fired power plants in the last 50 years, and its effect on the thermal efficiency and CO_2 emissions (based on information given in references [1–3]).

An improvement in operation conditions is only possible by enhancing the material properties of the components that are subjected to the harsh conditions in power plants (e.g. steam pipes and turbine parts). Excellent creep strength and corrosion resistance in combination with a good thermal conductivity and thermal expansion behavior are essential requirements for these materials to achieve intended lifetimes of 10 - 30 years [4]. Creep resistant martensitic Cr steels are found as the material of choice for this application. The use of modern 9 wt% martensitic Cr steels enables a maximum working temperature of 600 °C and pressure of 300 bar in ultra super critical power plants [2].

In order to apply the steels at 650 °C / 350 bar, which is believed to be the ultimate service environment for these steels [5], it is necessary to double the creep strength, and at the same time improve the corrosion resistance of the steels [6]. The development of a new generation of steels matching these requirements is the ultimate goal of this work.
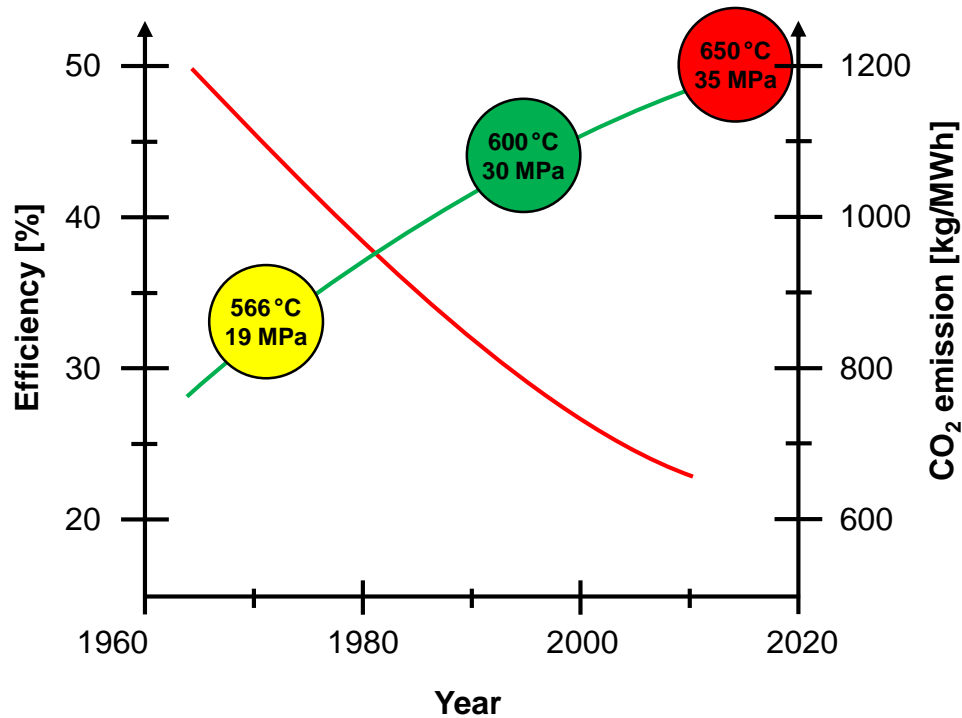
Figure 1.1: Change in operating conditions of power plants and its effects on efficiency (green curve) and CO_2 emission (red curve); based on information given in references [1–3].

1.2   Scope of this work

This work aims to develop a new generation of steels that enable working conditions of 650 °C / 350 bar. In order to meet this requirement, a new concept called *Z-phase strengthening* is applied, where the thermodynamically most stable phase in these steels (Z-phase) is used as the strengthening agent. Several trial steels have been developed in collaboration with the Technical University of Denmark. Two of these steels are characterized in this work. The focus of this thesis is to investigate the evolution of Laves phase, carbonitride and Z-phase particles during aging at different temperatures using scanning electron microscopy and atom probe tomography.

2   9-12 % Chromium steels

2.1   Basics about steels

Steels are iron carbon alloys that contain less than 2 wt% carbon. Depending on the total amount of alloying elements they are further divided into low-alloy (< 5 wt% alloying elements) and high alloy steels (> 5 wt% alloying elements) [7].

Iron is an allotropic element that has a body-centered cubic (bcc) structure below 912 °C (ferrite) and above 1394 °C (δ-ferrite). Between these temperatures, the face-centered cubic (fcc) structure (austenite) is most stable. Due to the polymorphism of FeC alloys and different solubilities of carbon in austenite and ferrite, a great variety of material properties and microstructures (ferrite, austenite, pearlite, cementite, martensite or bainite) can be achieved by changing the alloys' composition or the manufacturing parameters [8]. In general, since steels have good mechanical properties and they are relatively cheap compared to other material classes, they are the most used material in many applications.

Since pure iron is relatively soft, different mechanisms have been developed in order to increase its strength. Below, the five main strengthening mechanisms are discussed:

Solid solution hardening: Due to a difference in size and shear modulus between host and solute atoms (called misfit), elastic strain is generated. These internal stress fields can interact with the stress fields of dislocations and exert mutual forces. Depending on whether the solute atom is larger or smaller than the host atom, the solute atom will be moved to the tensile or compressive site of a dislocation, and thus an increased stress to move the dislocation is required [9]. In case of steels, the interstitial solutes C and N are the best solid solution strengtheners. Si, P, Mn and W are good substitutional solid solution strengtheners [10].

Work hardening is based on the interactions of dislocations with one another. The higher the dislocation density (e.g. due to plastic deformation) is, the higher the strength of a material. Besides the dislocation density and its distribution, the work hardenability depends also on the crystal structure, stacking-fault energy, strain rate and temperature. There is no effect of work hardening, when a material is annealed above its recrystallization temperature [9].

Grain boundary strengthening: Grain size is a very important material parameter affecting the strength as well as the toughness of steels. Whereas all other strengthen-

ing mechanisms lead to a decrease in toughness, it is increased by grain size refinement. Grain size refinement can be described by the Hall-Petch relationship: The yield stress is proportional to the inverse square root of the grain size [11].

Precipitation strengthening refers to interactions of dislocations with secondary phase particles or precipitates. In case of Cr-steels, this is the main strengthening mechanism. Typical precipitates (more details in section 2.3.1) are carbonitrides like MX (M = Ta, Nb or V; X = C, N) and $M_{23}C_6$ (M = Cr, Fe or W) or Laves phases (Fe_2M (M = W and/or Mo)) [12]. The dimensions, spacing between particles, lattice mismatch and the number of particles determine their interaction with dislocations. There are two mechanisms describing the strengthening due to particles.

If particles are impenetrable to dislocations, a dislocation will bow between particles and at a critical stress, segments of a dislocation with opposite Burgers vectors will annihilate and leave a dislocation loop around the particle. The smaller the distance between the particles, the higher is the critical stress needed for bowing a dislocation. This strengthening mechanism is described by the Orowan model [9].

Small (coherent) particles with low particle/matrix interface energy are penetrable to dislocations. In this case, particles get sheared by dislocations. The larger the particles are, the higher the stress needed for shearing the particles. If the particles get too large, the extra stress for shearing the particles is higher than the critical stress for bowing of dislocations between particles and the Orowan mechanism predominates [9].

Another positive effect of precipitates is that they allow controlling grain sizes. Particles pin grain boundaries and thus extra energy is needed to move grain boundaries away from the precipitates (Zener effect) [13].

Dispersion strengthening: Strengthening due to incoherent particles which are insoluble in the metal matrix – contrary to precipitates, which are soluble in the matrix at temperatures below the melting temperature. The strengthening effect can be explained by the Orowan model. In contrast to particle strengthened alloys, which are melted, cast and heat treated, dispersed particles are introduced via powder metallurgical techniques. Dispersion strengthened alloys maintain their strength up to very high temperatures in contrast to particle strengthened alloys. An example for dispersion strengthening in steels are oxide-dispersion strengthened steels [14, 15].

2.2   Creep and failure

Creep is a time dependent and thermally activated mode of plastic deformation of solid materials under mechanical stresses. In most metals and ceramics, creep becomes important at temperatures above half of their melting temperature (in iron: above 600 °C). If a structural component, e.g. a pipe in a power plant, is exposed to high pressures and high temperatures where creep becomes important, the pipe will expand and its thickness will permanently decrease. After a certain time, a critical thickness is reached, where the pipe cannot resist the inner pressure anymore and failure will occur.

Figure 2.1 shows two typical creep curves that are obtained when a specimen is subjected to a constant load at a certain temperature, and its elongation as a function of time is measured. These curves can be divided into three stages I, II and III [9]. As an elastic response on the applied load, creep curves start with an instantaneous strain. The first stage of the curves is called primary or transient creep and shows a high creep rate in the beginning that decreases until a stage with a constant creep rate $\dot{\varepsilon}$ (steady state) is reached. This stage II is called secondary creep and is followed by a rapid increase in creep rate until the specimen fractures (stage III). The decrease in creep rate in stage I is related to an increase in work hardening. In stage II, the process of work hardening is in balance with the recovery of the microstructure. Recovery refers to the processes that reduce the dislocation density or rearrange dislocations (e.g. into low energy sub-grain boundaries). These processes are thermally activated [16]. In stage III, a neck forms that increases the applied load locally and lead to an increased strain rate until specimen fracture.
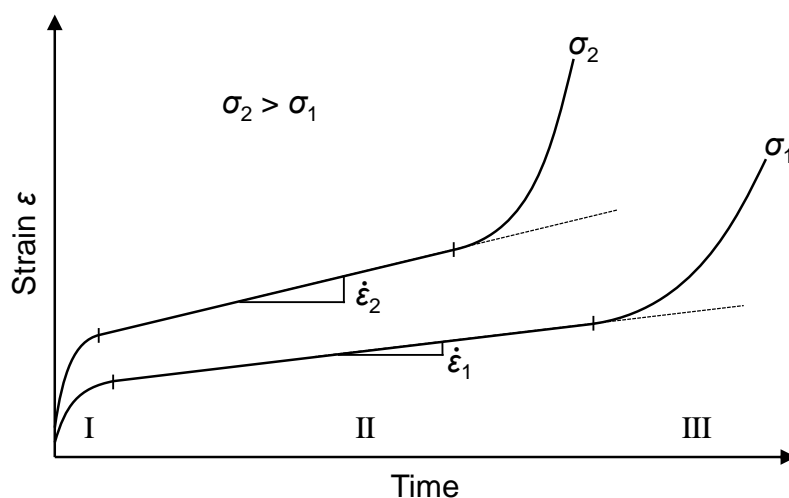
Figure 2.1: Schematic creep curves at constant temperature under constant loads σ_1 and σ_2.

As can be seen in figure 2.1, the shape of the creep curves depends on the applied load. A higher constant load σ_2 results in a higher creep rate $\dot{\varepsilon}_2$ and earlier fracture. The same behavior of the creep curves can be seen when varying the temperature. A higher temperature accelerates recovery and leads to a faster steady state creep rate. For practical applications it is important to design materials where the steady state creep lasts longer than the lifetime of the component.

Several mechanisms are responsible for creep. These depend on the temperature and the applied stress level. At low temperatures and stresses, creep is based on diffusion along grain boundaries and results in grain boundary sliding which is called Coble creep [17]. At higher temperatures, diffusion inside the grains becomes activated and leads to a flux of vacancies in a way that grains elongate in the direction of stress. This mechanism was proposed by Nabarro and Herring [18]. At high temperatures and stresses, dislocation (power law) creep is the mechanism responsible for creep. Due to the high temperature and the increased amount of vacancies, dislocations can overcome obstacles by climb and glide [9].

For heat resistant steels it is most important to shift creep to higher temperatures. This can be done by alloying steels with elements that retard the movement of dislocations or strengthen grain boundaries (cf. section 2.3.1).

2.3   Creep resistant 9-12 wt% Cr martensitic steels

Martensitic steels containing 9 wt% Cr are an important material class used in many applications at elevated temperatures and pressures. Good mechanical and thermal properties give a high operational flexibility. Additionally, low costs make these steels desirable for components like pipes or rotors in power plants. Nowadays, these steels allow maximum operational pressures of 300 bars at 600 °C [2, 19].

In order to further increase the efficiency and reduce the CO_2 emission of power plants, it is desired to increase the steam temperatures to about 650 °C. In terms of oxidation resistance, this can only be achieved by increasing the Cr content to 12 wt% Cr. However, this increase in Cr leads to an early breakdown in creep due to a micro structural phase transformation. Small MX carbonitrides, the main precipitation hardening agents in these steels (cf. section 2.3.1), transform to coarse Z-phase particles, which do not contribute to the creep strength (cf. figure 2.2) [19]. It is now tried to avoid premature failure of 12 wt% Cr steels by new alloy design [2].

The purpose of this section is to give a brief overview about the role of different precipitates and the alloy design of a 9-12 wt% Cr steel. In section 2.3.3, a relatively new alloy design concept called "Z-phase strengthening" is introduced, which is the concept behind the materials investigated in this thesis.
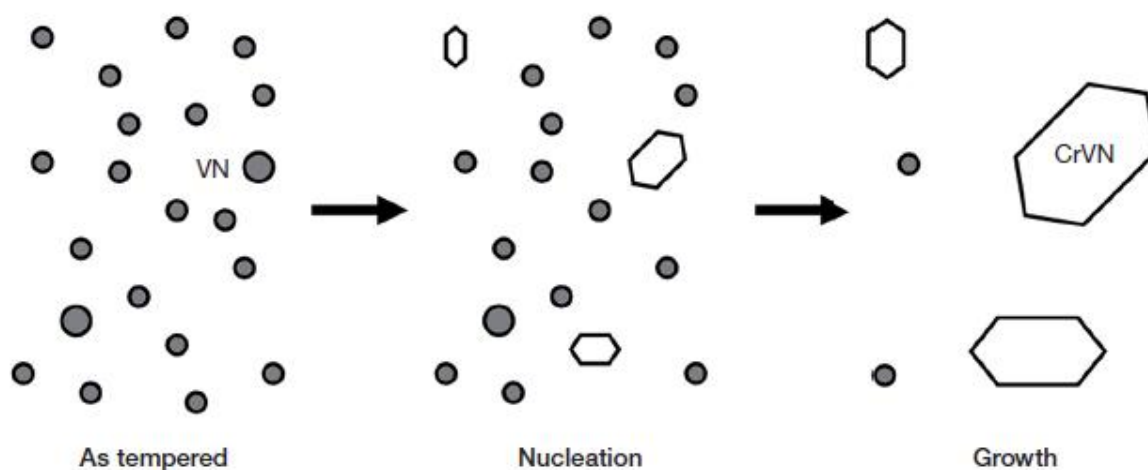
Figure 2.2: Principle of coarse Z-phase (CrVN) formation from fine MX (VN) particles leading to creep failure [19].

2.3.1   Precipitates

In 9-12 wt% Cr martensitic steels, a great variety of precipitates may form during tempering and subsequent high temperature service. Most of them strengthen or improve the creep strength of the steel but some of them weaken mechanical properties. Thus it is important to have a general understanding about the most important precipitates and their effect on the material properties. Precipitation reactions occur when a steel with a supersaturated solid solution is heat treated or aged at elevated temperatures. The precipitation process is divided into three stages: *nucleation*, *growth* and *coarsening*.

The *nucleation* process in solids is almost heterogeneous (on grain boundaries, stacking faults or other defects) and describes the formation of small stable nuclei from a supersaturated solid solution. The driving force for nucleation is a decrease in Gibbs free energy which increases with increasing undercooling. Since low temperatures reduce diffusion, the nucleation rate is highest at intermediate temperatures. Once a stable nucleus has formed, the growth stage starts [20].

During *growth*, the size of precipitates increases until the supersaturated matrix is in equilibrium. The temperature has an important influence on the precipitates size. If the temperature is very high, the nucleation rate is low and only a few nuclei will precipitate. Since diffusion is high, these nuclei will grow fast and will not provide any precipitation strengthening effects. In order to achieve a fine distribution of precipitates that provides additional strength, the nucleation rate has to be high [20].

Concerning the thermal stability of particle strengthened materials, the last stage of the precipitation process is the most important one. After nucleation and growth, the system still wants to achieve a state of minimum energy. By *coarsening* (Ostwald ripening) of some big particles in the expense of many small particles, the system reduces its interfacial free energy [21]. Since coarse particles do not provide any strength anymore, Ostwald ripening in particle strengthened materials has to be minimized. One way to reduce coarsening is to form particles with low interfacial energies (e.g. precipitates that are coherent with the matrix) [20].

The most important precipitates in 9-12 wt% Cr martensitic steels are:

$M_{23}C_6$: Particles with cubic crystal structure that mostly contain Cr and Fe. Furthermore, small amounts of Mo, W and B can be contained. $M_{23}C_6$ precipitates mostly at prior austenite grain and sub-grain boundaries and acts as obstacles for moving grain boundaries. Since $M_{23}C_6$ carbides are comparably large (200-300 nm) in diameter, their effect on strengthening the steel is relatively low. Furthermore, coarsening

of these carbides is a problem that has to be dealt with when designing the steel [22]. However, they are important to stabilize the boundaries.

MX carbonitrides (M = Ta, Nb or V) are coherent or semicoherent particles with a cubic NaCl type crystal structure, which mainly precipitate finely (2-20 nm in diameter) inside the matrix and strengthen the steel by pinning dislocations [22]. Since the solubility of Ta, Nb and V in the matrix is very low, MX precipitates coarsen very slowly and provide long term creep strength. In order to promote the formation of these fine precipitates, it is important to keep the C content low and control the formation of coarse primary MX carbides, which do not dissolve during austenitization and do not provide any precipitation hardening or creep strength [22, 23].

Laves Phase: The addition of W and/or Mo to the steels causes the precipitation of the hexagonal (C14) intermetallic Laves phase $(Cr,Fe)_2(W,Mo)$ (cf. figure 2.3). Laves phase precipitates mainly at prior austenite grain, packet and lath boundaries (cf. figure 2.4) [12]. Since W is depleted from the matrix by the formation of Laves phase, the solid solution strengthening effect of W decreases with time [24]. Furthermore, it has been shown that the formation of continuous Laves phase along grain boundaries significantly decreases the toughness [5]. On the other hand, Laves phase can contribute to the creep strength by retarding the recovery of sub-grain boundaries and compensate the loss in solid solution hardening by precipitation hardening, when precipitated as fine particles [24, 25]. Thus it is very important to control the distribution and morphology of Laves phase.

Z-phase: The thermodynamically most stable nitride in 9-12 wt% Cr steels is called Z-phase and has the empiric formula CrXN, where X is Nb, Ta or V [26]. Z-phase in general has a tetragonal crystal structure, as schematically shown in figure 2.3, and can also contain traces of Fe, Mo and of other elements [27]. Z-phase forms by picking up Cr from the matrix and diffusion of Cr into MX carbonitrides. After formation, Z-phase grows quickly. Experiments and calculations showed that the Cr content is the factor that influences most strongly the precipitation rate of Z-phase. The higher the Cr-content the higher is the driving force for Z-phase nucleation [26, 28]. In the case of martensitic steels containing 9 wt% Cr, the time for transformation of MX carbonitrides into Z-phase is longer than the lifetime of the components made of the steel. In 12 wt% Cr steels, this transformation is accelerated and takes place already during the service time of the components. This leads to creep failure, because coarse Z-phase particles do not provide any creep strength (cf. figure 2.2) [29]. Thus, the challenge in the development of 12 wt% Cr steels is to prevent the formation of coarse Z-phase particles (cf. section 2.3.3).

9

Laves phase

Z-phase

W or Mo

Fe or Cr

Cr

Ta, Nb or V

N
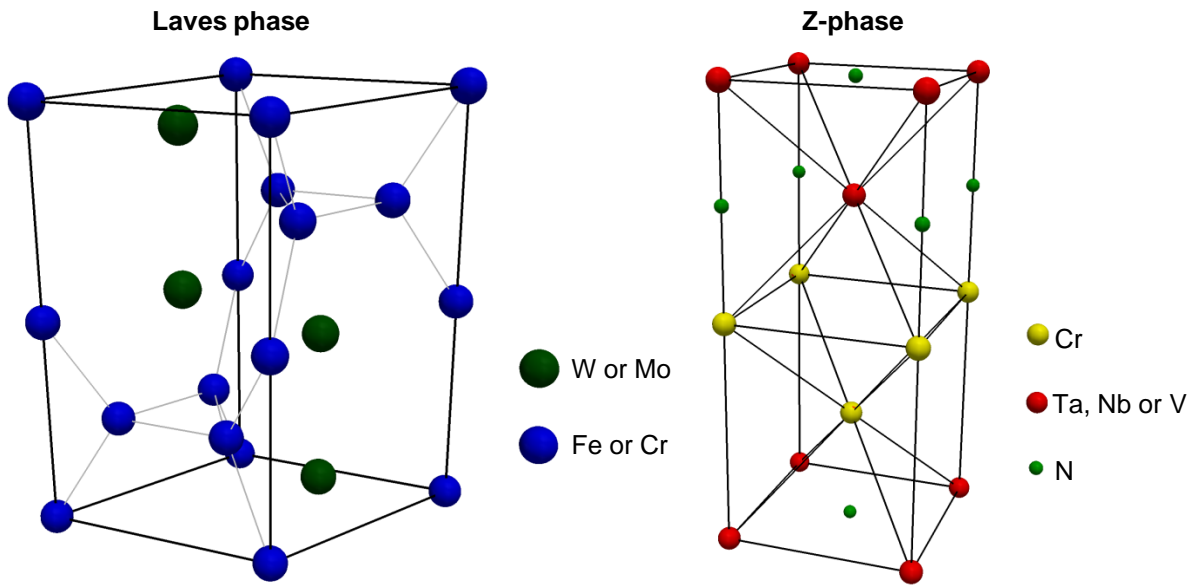
Figure 2.3: Schematic illustration of elementary cells: hexagonal (C14) structure of Laves phase (left image) and tetragonal structure of Z-phase (right image).

Block boundary

Packet boundary

Lath boundary

Laves phase

$M_{23}C_6$

MX

Prior austenite grain boundary
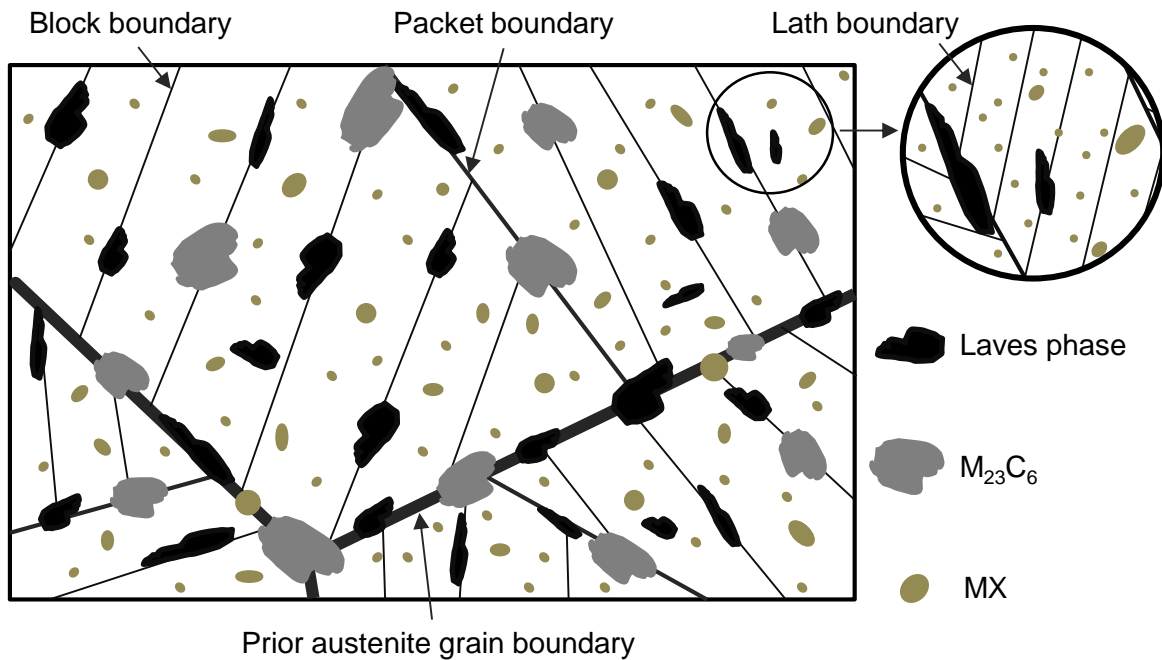
Figure 2.4: Schematic representation of the microstructure of 9-12 wt% Cr martensitic steels after tempering.

2.3.2 Alloy design

9-12 wt% Cr steels have the typical microstructure of tempered martensite. Martensite is the hardest phase that can be generated in steels and is the result of a diffusionless phase transformation [11]. By cooling steels from the austenite range to room temperature, ferrite becomes thermodynamically the most stable phase. If the cooling rate is too high, a diffusional phase transformation of austenite to ferrite cannot occur. With decreasing temperature, the driving force for a phase transformation increases. The consequence is a diffusionless phase transformation to martensite at a certain temperature (called martensite start temperature). Martensite has a body centered tetragonal structure and forms via shearing at an undistorted habit plane which is described by the Bain model [20]. The amount of carbon in the steel influences the morphology of martensite, hardness and amount of retained austenite. For low carbon steels, martensite forms laths with a high dislocation density, whereas at higher carbon contents a plate like martensite is obtained. The hardness of martensite increases with increasing amount of carbon but the toughness and the ability to form martensite during quenching (hardenability) decreases at the same time. In order to obtain optimum mechanical properties such as high yield and creep strength, hardness, toughness, formability and weldability in 9-12 wt% Cr martensitic steels, the amount of carbon is kept very low so that fine lath martensite with a high dislocation density is formed [11]. Lath martensite consists of small blocks that are arranged in packets (see figure 2.4) [9]. Since martensite is very brittle after quenching, martensitic steels have to be heat treated to increase their toughness. Thereby, the aforementioned particles (cf. section 2.3.1) precipitate and stabilize the microstructure.

9-12 wt% Cr steels contain10-12 alloying elements which optimize the steels' microstructure and mechanical properties at service conditions and environments. A Cr content of around 12 wt% is needed for the corrosion and oxidation resistance at 650 °C. For solid solution strengthening, W and Mo are added to the steels in low amounts (< 3 wt%). Higher contents lead to stabilization of δ-ferrite which is detrimental to the material properties. W and Mo further form Laves phase which can decrease the steels' toughness. Thus it is very important to control the formation, size, amount and morphology of Laves phase. One possibility is to add Cu [5]. Cu particles act as nucleation sites for Laves phase and thereby reduce the risk of continuous Laves phase layers along grain boundaries which significantly decrease the steels' toughness. The amount of the elements Si and Mn, which are mainly added for steel making purposes, is kept low to reduce the risk of embrittlement during tempering [9].

Nb and Ta in combination with C and N are essential to provide creep strength via precipitation strengthening. Ni, Cu and Co are austenite stabilizers and balance the effects of ferrite formers (Cr, Si, Mo, W, Nb and Ta) by e.g. inhibiting the formation of δ-ferrite [2]. Co additionally promotes the precipitation of Laves phase by lowering the solubility of W and Mo in the matrix [30]. Furthermore, by increasing the A_1 temperature, these elements allow tempering at higher temperatures [2]. Addition of B further increases the hardenability of the steel and stabilizes $M_{23}C_6$ particles [2].

2.3.3   Z-phase strengthening

In order to avoid premature failure due to formation of coarse Z-phase (cf. section 2.3), many new steels have been developed; mostly by aiming on thermally more stable MX precipitates or by alloying with elements that retard/delay the growth and coarsening of Z-phase [30]. Unfortunately, all these attempts failed for martensitic steels with more than 10.5 wt% Cr and service temperatures of 650 °C so far [31].

Since Z-phase is the most stable nitride [26] and all tries to delay its precipitation have failed, Danielsen and Hald proposed a new alloy concept called *Z-phase strengthening* in 2009 [19]. By increasing the driving force for Z-phase precipitation, a fast precipitation of Z-phase that is finely distributed is provoked. These small Z-phase particles provide strength via particle strengthening and furthermore, do not grow significantly, since the equilibrium concentration is reached very fast (cf. figure 2.5). First trial steels showed that this precipitation behavior could be obtained by substitution of V by Nb or Ta and by keeping the C content very low [19, 32]. Ta was thereby found as the most promising alloying element, since Z-phase formed fastest and most finely distributed [33]. Further investigations are now carried out on steels with industrially more feasible compositions. Two of these steels are characterized in this work and will be presented in the following section.
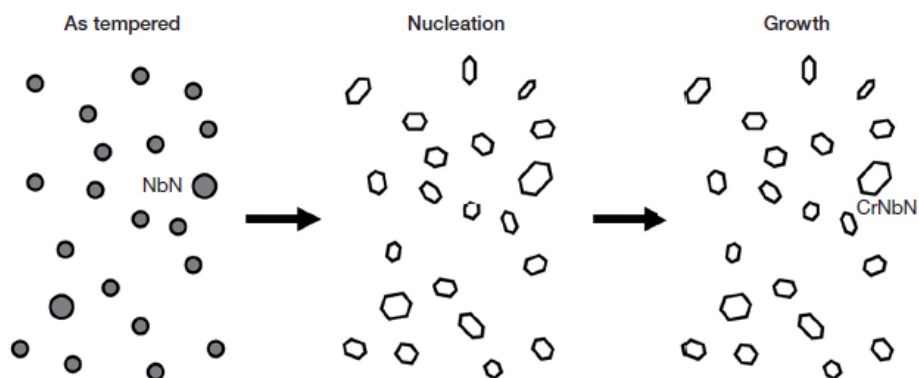
Figure 2.5: Principle of accelerated Z-phase (CrNbN) transformation (formation from fine MX (NbN) particles) and thereby obtaining a stable fine distribution of nitrides contributing to creep strength [19].

3 Experimental methods

In this section the investigated steels and experimental methods applied in this work are presented. The focus was on microstructural characterization via scanning electron microscopy and atom probe tomography. These techniques and specific sample preparation methods are explained in detail.

3.1 Investigated materials

In the scope of this thesis, two trial steels, 11Cr2.1W2Cu (ZU2) and 11Cr1.8W0.5Mo (ZU3), have been investigated. These steels belong to the third generation of trial steels that have been developed to meet the 650 °C challenge. Chemical compositions in weight and atomic percentage are given in table 1.

Table 1: Chemical composition of investigated steels (Fe in balance).

Steel		C	Mn	Si	Cr	Ni	Mo	W	Co	Cu	B	N	Ta	Nb
ZU2	at%	0.14	0.13	0.64	12.1	0.16	-	0.64	3.1	1.9	0.03	0.17	0.06	0.10
11Cr2.1W2Cu	wt%	0.03	0.13	0.32	11.2	0.17	-	2.1	3.2	2.1	0.005	0.042	0.19	0.16
ZU3	at%	0.24	0.12	0.47	12.2	0.20	0.3	0.56	3.0	-	0.02	0.15	0.14	-
11Cr1.8W0.5Mo	wt%	0.05	0.12	0.23	11.1	0.21	0.5	1.8	3.1	-	0.004	0.036	0.43	-

The aim of the third series of trial steels is to find the optimum ratio of carbon and nitrogen to achieve a fast transformation of MX to Z-phase particles. Furthermore, the boron content is kept low in order to minimize the formation of BN particles. Since the effect of combining Nb and Ta on the formation and coarsening of Z-phase is still unknown, trial steel ZU2 has been designed to investigate Z-phase precipitates based on Ta-Nb. Trial steel ZU3 has a higher carbon content and contains only Ta as a Z-phase forming element. Moreover it is tested, if alloying with Mo (Laves phase former) instead of Cu can be used to achieve a high toughness.

Both trials were produced via vacuum induction melting (VIM) and subsequent hot rolling into 20 mm thick sheets. Afterwards, they were austenitized at 1100 °C for 1 hour and quenched in air to room temperature. In the last step, they underwent double step tempering for 4 hours at 650 °C and 2 hours at 750 °C.

The trial steels were investigated after aging for 3, 7 and 31 days at 600 °C, 650 °C and 700 °C. Therefore, all specimens were cut with a low speed saw into slices for consecutive APT, SEM and TEM (not in the scope of this thesis) investigations.

3.2 Scanning electron microscopy

In this work a scanning electron microscope (SEM) was used to investigate the microstructure of steels ZU2 and ZU3; in particular Laves phase particles, in order to obtain their volume fraction and compositional information. In addition it was also used to check the quality of atom probe samples.

Resolution in an optical microscope is limited by the wavelength γ of the incident beam which is described by the Rayleigh criterion [34]

$$\delta = \frac{1.22 \cdot \gamma}{NA_o + NA_c} \; , \qquad\qquad [2]$$

where δ is the smallest resolvable distance of two objects and NA_o and NA_c are the numerical apertures of objective and condenser. Thus, optical microscopes that use visible light as an incident beam, allow resolving objects with a size of several hundreds of nm. This resolution power is too little to resolve the particles and atom probe samples investigated in this thesis. By using electrons as an incident beam, much better resolution can be obtained. In electron microscopes lens imperfections limit the resolution. The spot size is the most influencing factor and limits the image resolution to about 1-5 nm in modern SEMs. The challenge is to produce a beam with a minimum spot size that impinges enough current upon the specimen in order to generate the various imaging signals.

The working principle of an SEM and how it was used in this thesis is the content of this section. The information provided are mainly based on J. Goldsteins book "Scanning Electron Microscopy and X-Ray Microanalysis" [35]. Other references are also cited accordingly.

3.2.1 Working principle

An SEM consists of two parts: the electron column and the control console. At the top of the electron column an electron gun generates electrons that are accelerated downwards to an energy of 0.1 keV - 30 keV, focused and deflected onto the specimen, which is located below the column. The whole column is under high vacuum. There are three common types of electron sources. They are tungsten, lanthanum hexaboride and field emission guns (FEGs). These guns differ in the size of the electron source. Whereas tungsten and lanthanum hexaboride guns have a source size of several micrometers and emit electrons as a hot cathode, in FEGs electrons tunnel out of the cathode due to the high electric field generated at the source that is in the

form of a sharp needle (in the range of some nanometers). FEGs generate very coherent beams with high brightness but less stable emission currents compared to thermionic emitters. In this work, a Schottky field emission gun was used. Schottky emitters are sharp tungsten needles coated with a monolayer of zirconium oxide which lowers the work function of tungsten from 4.5 eV to 2.8 eV, and thus enables a working temperature of around 1800 K. At this temperature residual gases in the column are not absorbed by the source. Therefore, this enables a more stable emission current than cold field emission guns that work at ambient temperatures.

SEMs use electromagnetic lenses to focus the electron beam to a small spot by means of the Lorentz force. These lenses are far from being perfect since they cause aberrations and astigmatism which limit the resolution in a SEM and thus have to be corrected. Electrons far away from the optical axis of a lens experience a higher Lorentz force and are therefore bent stronger (spherical aberration). This problem can be dealt with by using a small aperture that blocks the outer part of the beam. Also electrons with varying energies experience different forces, which results in chromatic aberration. By using a field emission gun that generates a very coherent electron beam, this aberration is minimized. If the magnetic field of the lens is not perfectly homogeneous (e.g. due to asymmetric lenses), the focused beam will not be cylindrical, which leads to a blurred image. This lens error is called astigmatism and is corrected with a stigmator, an octupole of electromagnetic coils, which is controlled by the operator to apply additional magnetic fields in appropriate directions.

When the electron beam interacts with a specimen, different signals are generated that can be detected by corresponding detectors and are used for imaging or chemical analysis (cf. figure 3.1). One distinguishes between elastic scattering and inelastic scattering. Elastic scattering means that electrons get deflected without losing kinetic energy. After several events, electrons might get scattered backwards out of the specimen. These electrons are called backscattered electrons (BSE). They give an atomic number contrast (Z contrast), since heavy atoms have a higher probability to scatter electrons back. Electrons may also lose kinetic energy during scattering, which is called inelastic scattering. In this case, electrons of the primary beam lose energy by transferring their energy to electrons of the specimen. If this energy is high enough, outer shell electrons get emitted. These are called secondary electrons (SE) and have an energy of less than 50 eV [36] (cf. figure 3.2). Due to their low energy, they get absorbed very fast by the specimen and their probability to leave the surface decreases exponentially with depth. SEs are emitted only from the first few nanometers of a specimen. They give topographical contrast.
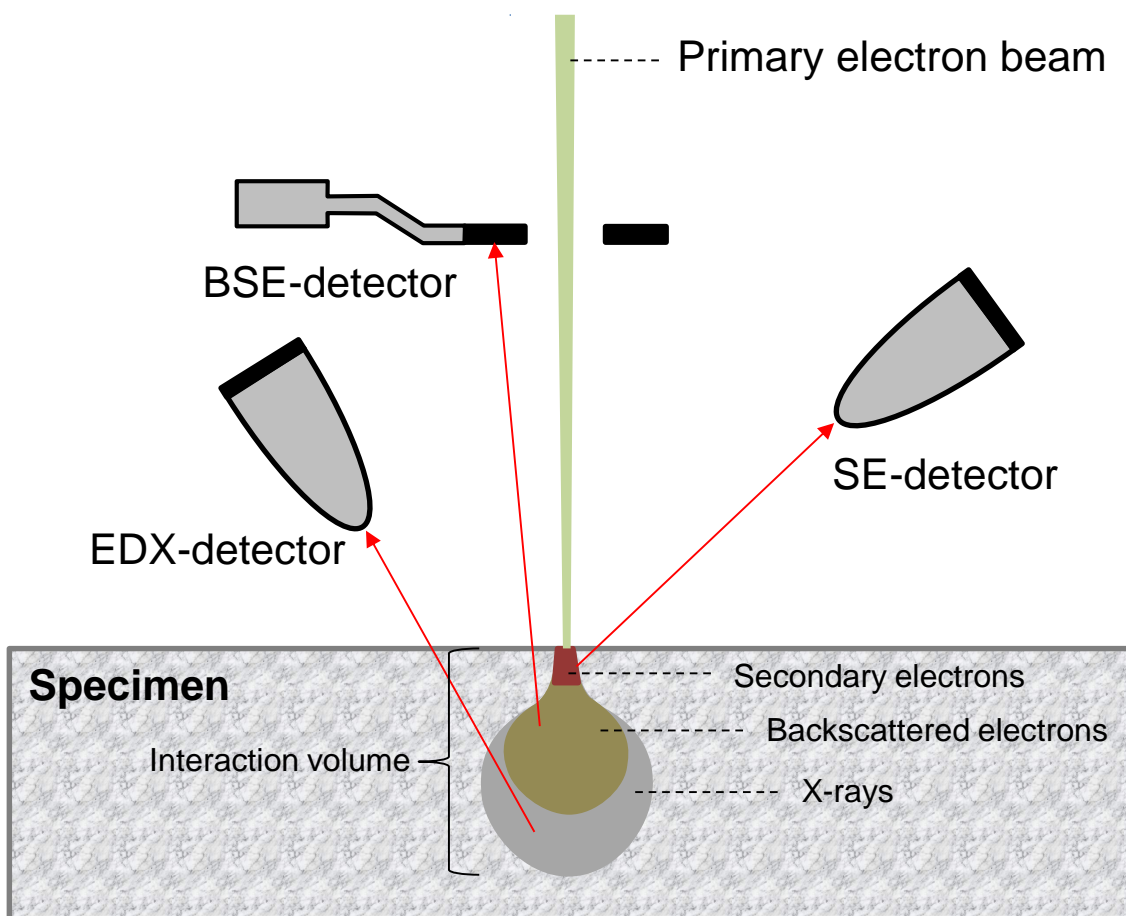
Figure 3.1: Schematic drawing of an electron beam in a SEM interacting with a specimen and several frequently used detectors catching the signals.
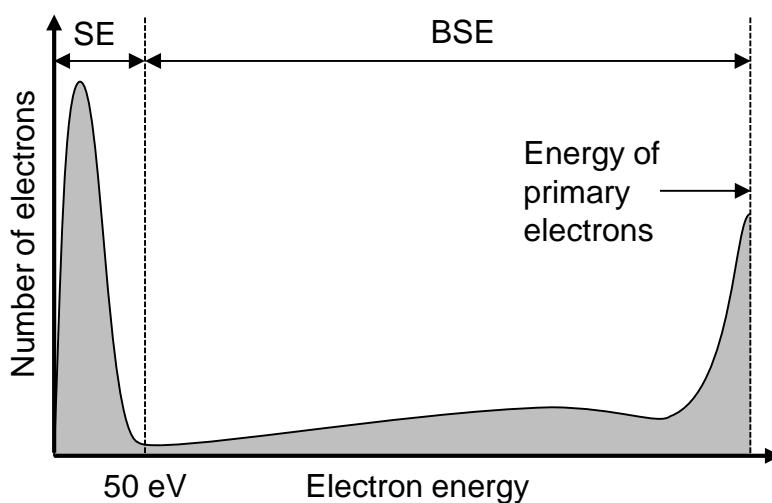
Figure 3.2: Schematic spectrum of the energy distribution of scattered electrons.

It can also happen that tightly bound electrons from inner shells get ejected. In this case, electrons from outer shells will fill the vacancies by emitting photons with characteristic energies according to the energy difference of the involved electron shells. These photons are characteristic for each element, which allows to determine the chemical composition of the specimen by energy dispersive X-ray spectroscopy (EDX). X-rays can be detected from depths up to two micrometers and have the largest interaction volume of all signals generated by the primary electron beam.

3.2.2 Sample preparation and experimental procedure

The specimens were embedded in a conductive resin and subsequently ground using SiC paper (grit steps from 400 to 4000) and polished using diamond suspension until 1 µm. After cleaning, the specimens were fixed on a SEM specimen stub with a carbon tape and finally investigated with a Leo Ultra 55 FEG SEM.

SEM BSE micrographs were obtained using a four-quadrant solid state backscattered electron detector (QBSD), since the contrast between Laves phase and matrix was highest using this detector. In order to quantify particles, micrographs were taken in sequences of 5x5 or 5x6 images with an accelerating voltage of 7 kV and a working distance of 6.7 mm as schematically shown in figure 3.3. For accurate measurement of particle sizes, the first image of every sequence was additionally taken with a standard Everhart-Thornley SE detector. Compositions of particles were identified by the combined use of the QBSD and the EDX detector with an acceleration voltage of 13 kV and a working distance of around 10 mm.
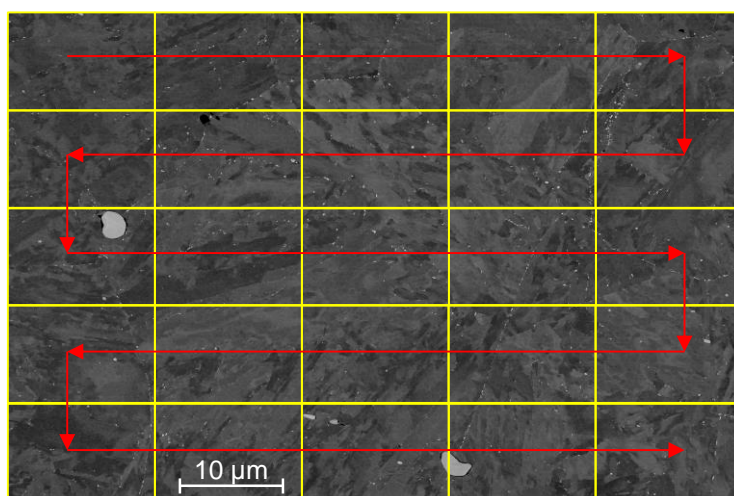
Figure 3.3: Schematic drawing showing how image sequences were taken.

3.3 Image analysis

For SEM image analysis, a technique analog to that used by Korcakova et al. [37] has been applied. This was done using the software *ImageJ*. In the first step, the image sequence was cropped and binarized. Afterwards, a threshold value was set by overlaying one BSE image of the sequence with the corresponding SE image (cf. figure 3.4). This procedure minimizes the probability of over- or underestimating particle sizes.

Sometimes, several particles are connected to one big particle in BSE images. Since *ImageJ* would count these particles as one particle, the *watershed* algorithm of *ImageJ* was applied, that automatically separates these particles as schematically shown in figure 3.5.

Then the particle analysis function of *ImageJ* was used to automatically measure the particle sizes by overlaying particles with best fitting ellipses. In order to minimize systematic errors, a minimum particle area corresponding to an equivalent circle diameter of four pixels was chosen. From the measured areas A of Laves phase particles, equivalent diameters d_m were calculated by

$$d_m = 2 \cdot \sqrt{A\pi} \quad . \tag{3}$$

Since the threshold value for Laves phase particles was chosen according to SE images, the equivalent diameter has to be corrected for truncation. Assuming a plain truncation of precipitates, the corrected equivalent diameters d_{cor} are calculated from reference [38]:

$$d_{cor} = \frac{4}{\pi} \cdot d_m \tag{4}$$

In a last step, all particles that could clearly be identified as MX precipitates (particles with a perfect circular shape) have been removed manually from the results list. From this list, mean equivalent diameters, area fractions and particle densities have been calculated. Mean diameters were obtained by excluding particles that lie on edges of the image. For the calculation of the particle densities, particles on edges have been counted as half particles.
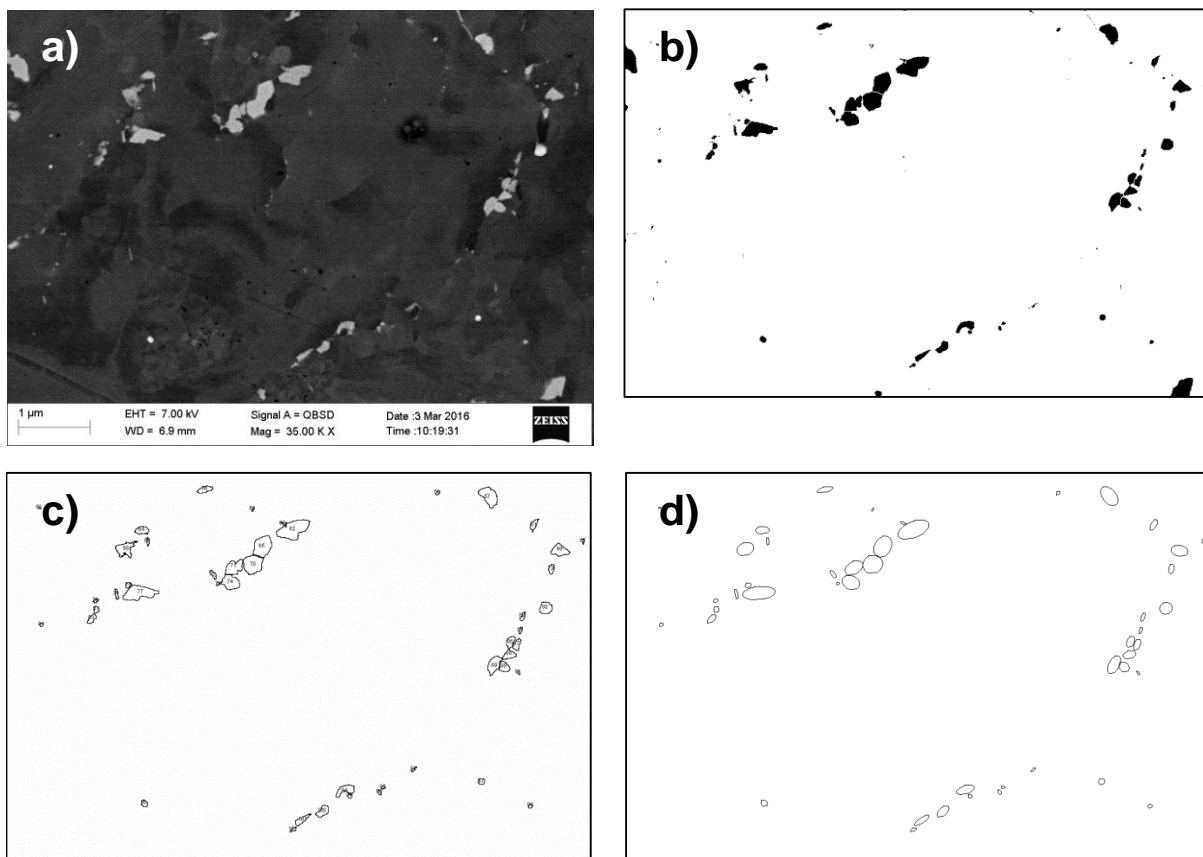
Figure 3.4: Image analysis with *ImageJ*: a) SEM BSE micrograph (Laves phase exhibits a bright contrast); b) Micrograph after setting a threshold value (Laves phase is now black); c) Analyzed particles outlined and numbered; d) Analyzed particles showing best fitting ellipses.
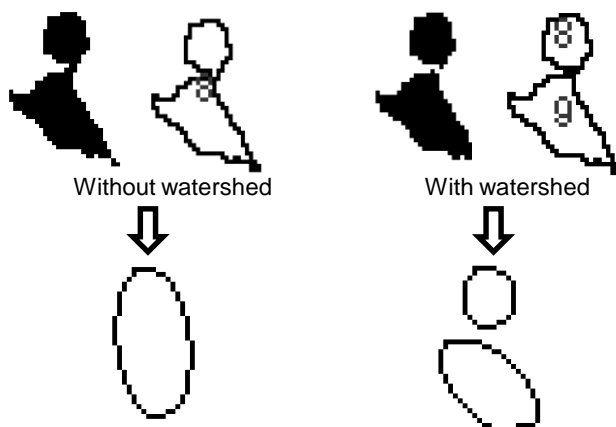
Figure 3.5: Scheme of particle analysis with *ImageJ* with (right) and without (left) the use of the watershed algorithm.

3.4   Atom probe tomography

In this thesis atom probe tomography (APT) was used to analyze the trial steels on an atomic level in three dimensions. By controlled field evaporating atoms from a needle-shaped specimen and collecting the ions with a detector, chemical compositions and information about sizes of precipitates can be obtained. This section aims to explain the basics about APT and how the technique was applied in this thesis.

3.4.1   Working principle

Field evaporation:

Atom probe tomography is based on the principle of field evaporation. The phenomenon of field evaporation can be described in a simplified way with a one-dimensional potential energy diagram (see figure 3.6) according to the *Image-Hump-Model* of M.K. Miller [39]. Without an applied electric field, ionic states of surface atoms are instable, since neutral states are energetically more favorable. By applying an external electric field, the potential curve for the ionic states gets lowered and can cross the curve of the neutral states at a certain distance from the surface. At this distance the ionic states become more stable. Via thermal activation above the maximum of the ionic potential curve (so called Schottky Barrier), it is possible to evaporate a surface atom [39, 40].

In order to evaporate atoms under common experimental conditions, electric fields in the order of several 10 Vnm^{-1} are needed. Since the electric field E on a sample is proportional to the voltage U and the inverse of the radius r of the sample, it is possible to achieve these fields by using needle shaped specimens with a tip radius between 10 nm and 50 nm and applying a voltage of several kilovolts.

$$E = \frac{U}{\beta \cdot r} \qquad\qquad [5]$$

In this formula β is the so called field factor, a geometric factor that describes the reduction of the electric field due to the shaft of the specimen [41].
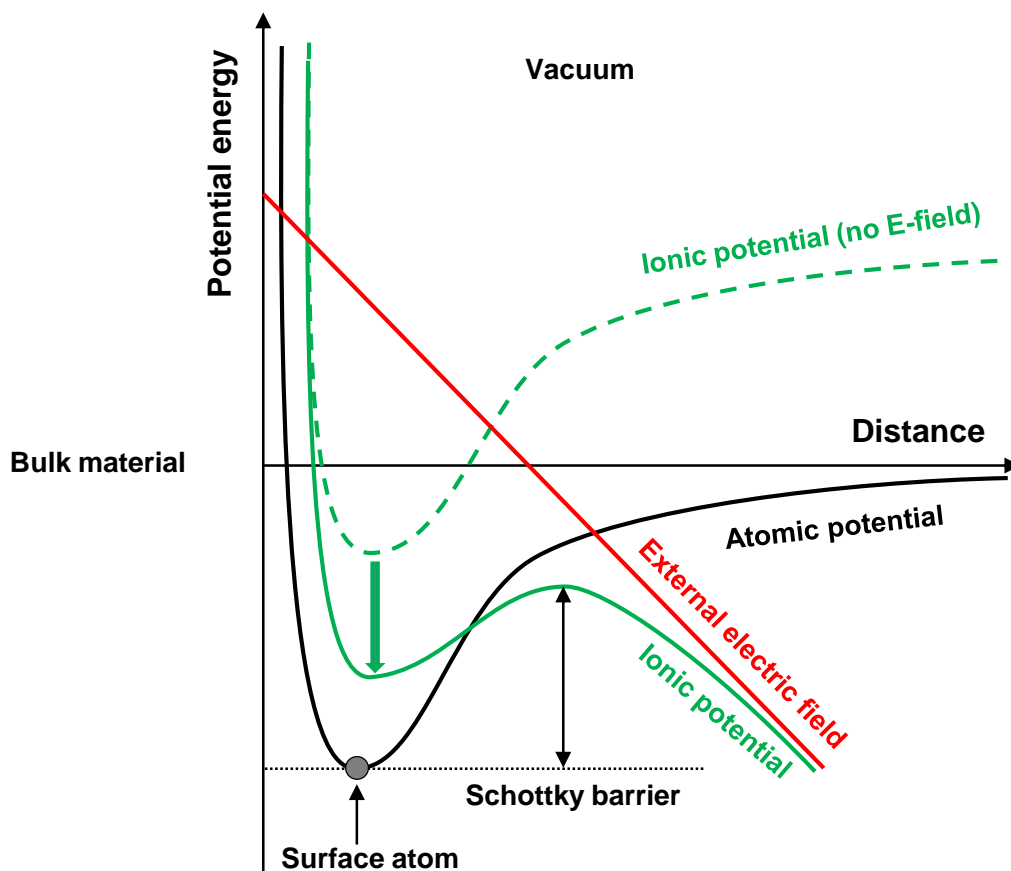
Figure 3.6: Potential energy diagram of a surface atom with and without applied external electric field.
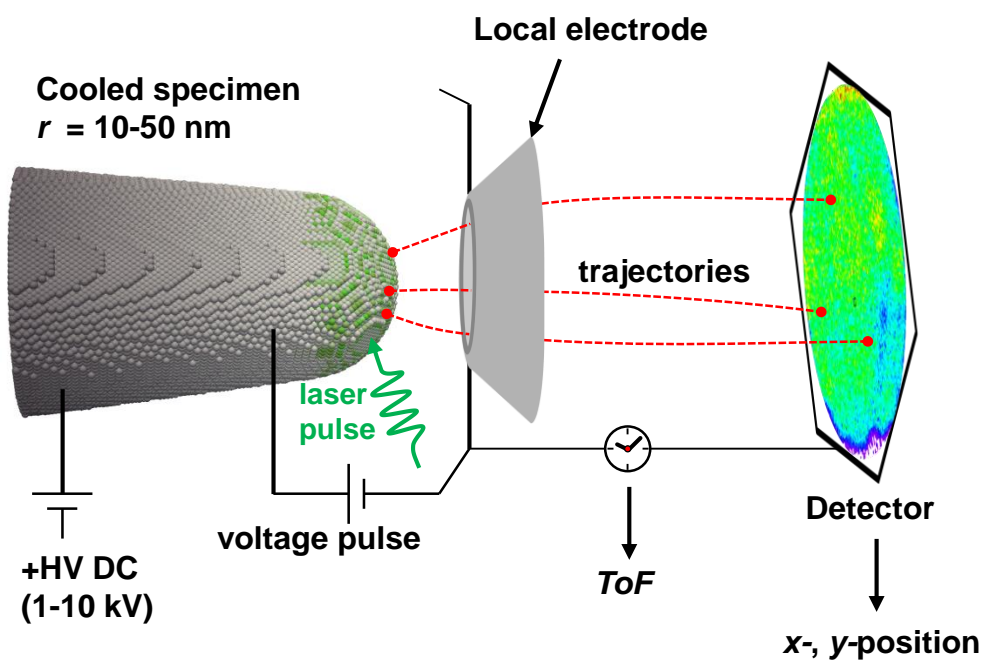
Figure 3.7: Schematic illustration of the setup of a local electrode atom probe (LEAP). Either laser or voltage pulses can be used for controlled evaporation of atoms.

Experimental setup:

Figure 3.7 shows schematically the basic setup of an APT measurement. All details about atom probe tomography provided in this section are based on information given in the *Local Electrode Atom Probe Tomography* user's guide of Larson et al. [42]. The needle shaped specimen is placed in an ultra high vacuum chamber in most cases in front of a grounded or negatively biased detector. The specimen is cooled to cryogenic temperatures (20 K - 80 K) in order to reduce the thermal motion of atoms leading to positional errors. A high standing positive DC voltage which is chosen in a way that no field evaporation will occur is applied to the specimen. Only by using nanosecond voltage or laser pulses, surface atoms begin to evaporate at known time points. Voltage pulses are either positive electrical pulses on the specimen or negative pulses on a counter electrode that is placed in front of the specimen. The amplitude of the pulses, known as pulse fraction, is around 10-30 % of the standing voltage. Instead of voltage pulses also laser pulses with an energy in the range of 0.1-0.5 nJ can be used. This is done especially for non conductive specimens. The laser increases the temperature of the specimen locally by 100-300 K. This rise in temperature decreases the evaporation field leading to ionization of atoms (cf. figure 3.8).
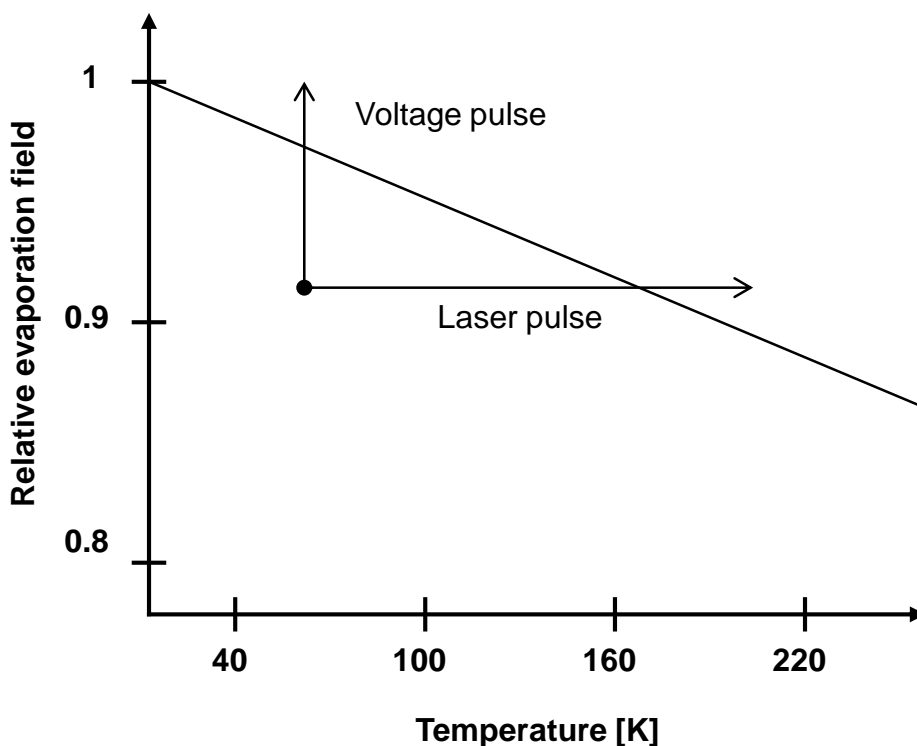
Figure 3.8: Schematic showing the relative field of evaporation as a function of temperature and the influence of voltage or laser pulses.

The advantages of laser pulses are a higher mass resolution and larger analysis volumes, since voltage pulses cause stresses that often lead to premature failure [43]. On the other hand, the increased temperature due to the laser pulses leads to a degradation in spatial resolution due atomic thermal motion [42]. The rate the pulses are generated amounts around 200 kHz [42]. During operation, the standing voltage is set in a way that for only 0.2-0.5 % of the pulses one atom is ionized (set-up called evaporation rate), since higher evaporation rates cause more multiple hits on the detector and increase field induced stresses which may lead to premature fracture.

After field evaporation, ions are repelled perpendicular to the specimen surface and then accelerated by the electric field in direction of a position sensitive detector. By measuring the time between pulse and the signal of an incoming ion on the detector, the time of flight (*ToF*) and the *x* and *y* coordinates on the detector are registered.

In this work a local electrode atom probe (LEAP), that was additionally equipped with a reflectron unit, was used for APT measurements. This instrument can be characterized by the cone shaped local electrode which is placed only a few micrometers in front of the specimen (cf. figure 3.7) and the energy compensator (reflectron), which minimizes the energy spread of field evaporated ions and increases their flight paths (not shown in figure 3.7). These modifications improve the quality of APT measurements significantly. The local electrode close to the specimen enhances the electric field by factor 10 and allows lower voltages for field evaporation. This enables a larger field of view (up to 200 nm), meaning larger analyzed volumes, and it improves the mass resolution by a reduction of the energy spread of ions (due to lower voltages). Furthermore, lower voltages increase the data collection rate, since it is easier to generate uniform voltage pulses with a lower energy. Thus, the pulse frequency is only limited by the time of flight, which has to be shorter than the time between two pulses. The reflectron unit compensates the energy of ions by forcing ions with slightly higher energy to take longer pathways to the detector [44]. In the idealized case, all ions with the same mass to charge ratio have the same time of flight, resulting in a very high mass resolution power of greater than 1000. The disadvantage of a reflectron is a loss in detection efficiency.

Mass spectrum:

By knowing the distance between specimen and detector *L*, the time of flight (*ToF*) and the voltage applied for field evaporation *V*, the mass *m* to charge state *q* ratio can be calculated in terms of classical physics based on Newton's equation of motion:
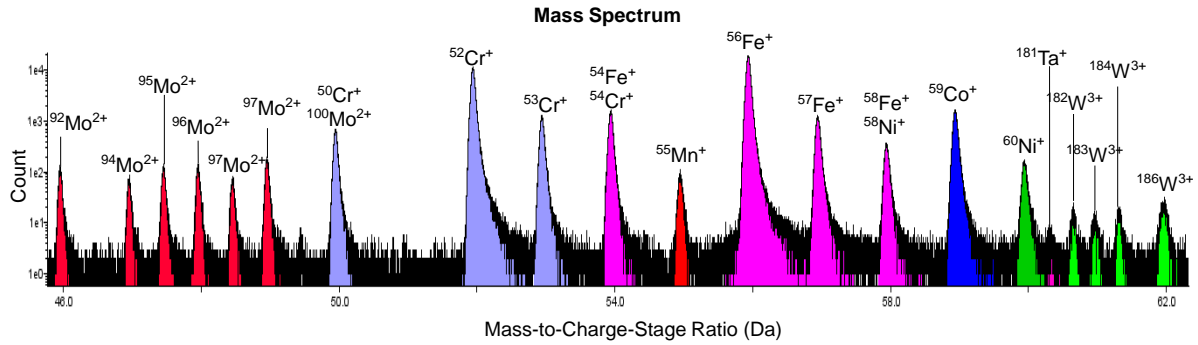
Figure 3.9: Part of the mass spectrum of steel ZU3 with identified peaks.

$$\frac{m}{q} = 2eV \cdot \left(\frac{ToF}{L}\right)^2,$$ [6]

where e is the elementary charge [42]. The mass to charge ratio enables to identify the type of each ion. By plotting the number of detected ions as a function of their mass to charge ratio, a mass spectrum as shown in figure 3.9 is obtained. The high mass resolution of APT measurements allows to differentiate between single isotopes. Since there are 12-13 different elements in the investigated steels, overlaps of certain peaks may occur (e.g. $^{54}Cr^+$ and $^{54}Fe^+$). This issue can be solved by software that statistically decomposes overlapping peaks. In order to further improve the mass resolution, *ToF* corrections are applied which take into account that flight paths differ as a function of the detector hit location [42].

Reconstruction:

The scientifically most exciting feature of APT is the ability to reconstruct the specimens' three dimensional atomic volume from the two dimensional detector signals. In principle, there are two different techniques for reconstructing atom probe data. These techniques differ in the input parameters. One technique uses a predefined sample shape as an input parameter; the other uses the voltage and the evaporation field for calculating three dimensional atomic positions. The latter is the most common one, and is applied in this thesis. Several reconstruction protocols can be found in literature. In the following context, the simplified approach described by Blavette [45] and applied by Bas et al. [46] will be explained in more detail.

The first step is calculating a magnification M that converts the 2D detector positions x_D and y_D into real space coordinates x and y. Assuming the detected ions are point projected, the magnification M is calculated dividing the specimen-detector distance L by the radius of the specimens' curvature r. Since the specimen has the

24

shape of a half sphere and trajectories are bent into the direction of the detector, a so called image compression factor ξ has to be included in the equation, which reduces the magnification [47]:

$$M = \frac{L}{\xi \cdot r}$$ [7]

With equation [5] describing the electric field around an apex, magnification M can be calculated for every ion directly from the input parameters:

$$M = \frac{L \cdot E \cdot \beta}{\xi \cdot U}$$ [8]

Since iron is the element with the highest concentration in the investigated steels (more than 80 at.-%), the evaporation field of iron of 33 Vnm^{-1} has been used for variable E [48]. Field factor β is in the range of 2 to 5, but often it is unknown before atom probe analysis. Thus, the magnification is not very accurate and dimensions in atom probe reconstructions have to be treated carefully. The magnification can be calibrated by using crystallographic features within the tomographic reconstruction to find a correct value for β [42]; e.g. by comparing atomic plane distances in the reconstruction with crystallographic ones.

The magnification enables to calculate the space coordinates x and y:

$$x = \frac{x_D}{M} \quad \text{and} \quad y = \frac{y_D}{M}$$ [9]

In a last step, the depth coordinate z is calculated. It is assumed, that ions evaporate from the specimen surface which is located at a certain depth z_{tip}. By evaporation of ions, z_{tip} is shifted by a small increment Δz for each ion. Δz increases by one atomic volume Ω divided by the analyzed area on the specimen S_A per evaporated ion:

$$\Delta z = \frac{\Omega}{\eta \cdot S_A}$$ [10]

η is the detector efficiency which takes into account that not all evaporated atoms can be detected. The detected area S_A is the region of the specimen surface which lies in the field of view and can be seen as the reverse projection of the detector area S_D to a plane tangential to the specimens' apex:

$$S_A = \frac{S_D}{M^2}$$ [11]

Combining equations [8], [10] and [11], the depth increment Δz is:

$$\Delta z = \frac{\Omega \cdot (L \cdot E \cdot \beta)^2}{\eta \cdot S_D \cdot (\xi \cdot U)^2}$$ [12]

In order to take into account that the specimens' curvature is half sphere like, a corrective term $\Delta z'$ has to be added for each ion, which projects the atomic positions from the tangential plane at the specimens' apex orthogonally to the tips' surface:

$$\Delta z' = r \left(1 - \sqrt{1 - \frac{x^2 + y^2}{r^2}} \right)$$

[13]

Extensions of this protocol take the specimens shaft into account and can be applied for wider fields of view (cf. Geiser et al. [49] and Gault et al. [50]).

3.4.2 Sample preparation

The aim of the sample preparation is to produce needle like specimens with a final tip radius of 10 nm - 50 nm. This was done by electropolishing which is the most common technique to produce APT specimens out of metals. In order to prepare the samples for electropolishing, sheets were cut with a low speed saw into rods with a size of around 300 µm x 300 µm x 1.5 mm. These rods were clamped into aluminum holders. Afterwards electropolishing was performed in three main steps. The experimental assembly was the same in all steps. The specimens were connected as anode to a power supply using a DC voltage of 20 V. As cathode, a gold wire in the form of a loop was used (cf. figure 3.10). The middle of the specimen was placed in the center of the loop. The first electropolishing step aims to form a neck with a diameter of several micrometers. Therefore, a strong electrolyte containing 10 % perchloric acid, 20 % glycerol and 70 % methanol was filled on top of an inert liquid (here 1,1,2-trichloroethylene) so that the end of the specimen dipped into the inert liquid. After formation of the neck, a weaker electrolyte with 2 % perchloric acid in buthoxyethanol (without an inert liquid) was used to electropolish until the lower part of the specimen dropped off. A special device was used that stopped the power supply at the moment the specimen was divided into two pieces. The part of the specimen that fell down was then picked up and also clamped in an aluminum holder. In a third step, both specimens were backpolished. That was done using the same electrolyte as used for step 2, but with a voltage pulse generator as power supply. Then, pulses with decreasing pulse length from 5 ms to 5 µs were used. Backpolishing was performed since it produced samples with a smoother surface that resulted in more stable APT runs and higher yields. In the end the samples were washed in ethanol, dried and imaged with the SEM regarding the final shape (cf. figure 3.11).
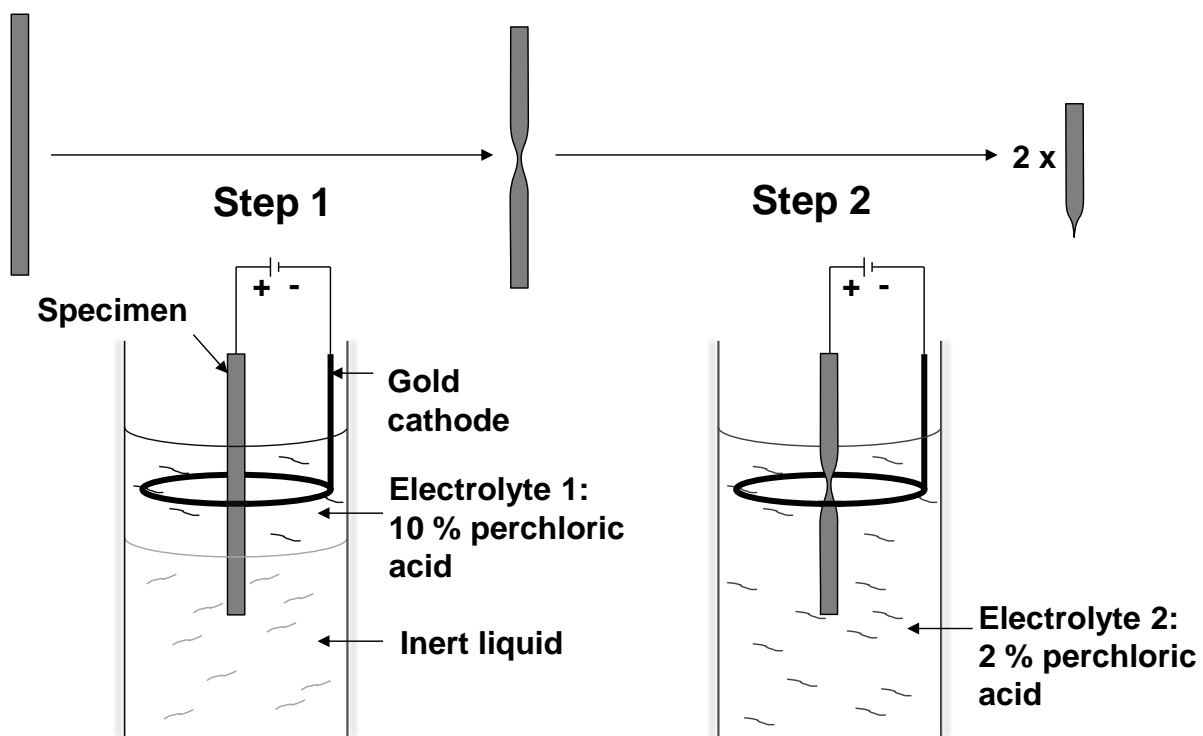
Figure 3.10: Schematic showing the principle of preparing APT specimens via electropolishing; step 1: forming a neck; step 2: electropolish until the lower part of the specimen drops off.
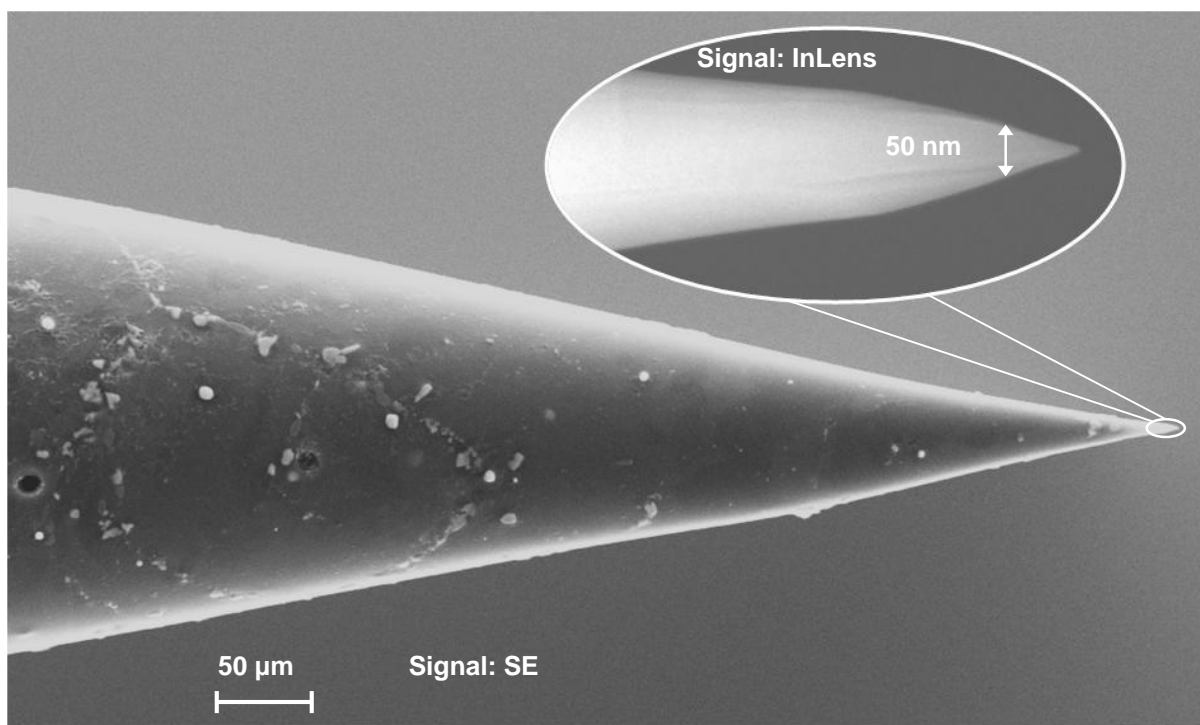
Figure 3.11: SEM images (low and high mag.) of an electropolished specimen after post sharpening via FIB milling.
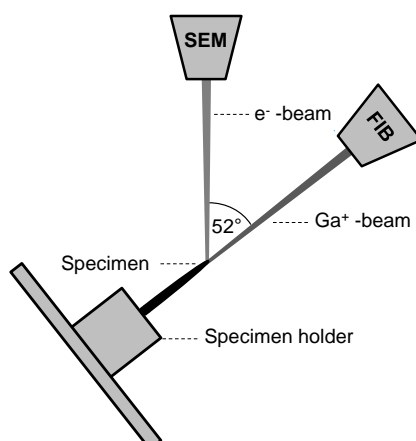
Figure 3.12: Schematic drawing of an FIB-SEM used for annular ion milling.

Samples that were not sharp enough have been post sharpened using a technique called focused ion beam (FIB) milling. The working principle of an FIB device is in general the same as the one for an SEM, but with the difference that Ga ions are used instead of electrons. Ga ions are heavy in comparison to electrons and can be used for imaging and additionally in order to sputter atoms of the sample away. In this work a Versa 3D LoVac^{TM} of *FEI* was used for FIB milling. This device is equipped with both, an FIB and an SEM, which enables in situ observations of the milling process (cf. figure 3.12). The specimens have been ion milled using an annular milling pattern, a voltage of 10 kV and decreasing currents until a final diameter of around 50 nm was achieved.

FIB milling was partly also used with the aim to have particles at the specimens' tip, which could be later analyzed with the atom probe. This was done by removing material and insitu observation with the SEM, until the particle was within the first few hundred nanometers of the specimen.

3.4.3 Experimental procedure

For APT measurements, an Imago LEAP 3000X HR was operated by both, voltage and laser pulsing, with a pulse frequency of 200 kHz. For voltage pulsing, the specimen was kept at a temperature of 70 K using a pulse fraction of 20 % and an evaporation rate of 0.2 %. For laser pulsing, the specimen was kept at a temperature of 55 K using a laser energy of 0.3 nJ. The evaporation rate was set to 0.2 % until the measurement ran stable and then increased to 0.5 % or even higher.

For reconstruction and analysis, the IVAS^{TM} software by CAMECA$^{®}$ was used as is described in the next section in more detail.

3.5   Analysis of atom probe data sets

APT analysis was performed with the focus on the evolution of the steels' matrix and particle chemical concentrations during aging at different temperatures. After 3D reconstruction with IVAS™ the reconstructed data sets were analyzed to reveal possible variations in concentrations of certain ions. This was done by either comparing reconstructed volumes with only one sort of ions (cf. figures 3.13 b) and 3.14), by using 1D concentration profiles and/or by using isosurfaces.

3.5.1   Matrix compositions

Compositions of the matrix were analyzed from volumes inside the reconstructed data set that are free from particles and grain/lath boundaries (cf. figure 3.13 c)). Grain/lath boundaries can be detected by visualizing C or B ions as shown in figure 3.13 b), since these ions segregate preferentially at these boundaries. A cylinder shape was used to extract a volume of matrix. After a final optimization of the range file for the peaks in the mass spectrum, matrix compositions are calculated using the automated decomposition of peaks. The matrix compositions are presented and discussed in section 4.2.1.
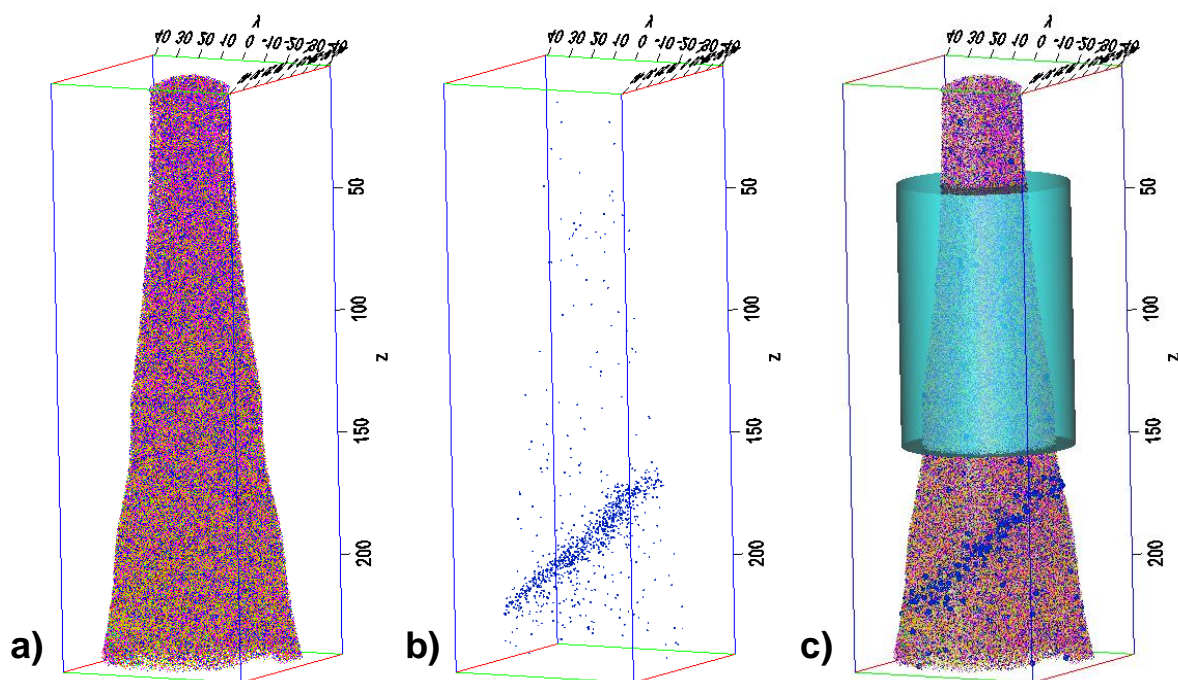
Figure 3.13: Reconstructions of an APT data set showing: a) all ions; b) only B ions; c) cylinder that is used to extract volume for matrix composition; the scale is in nanometers.
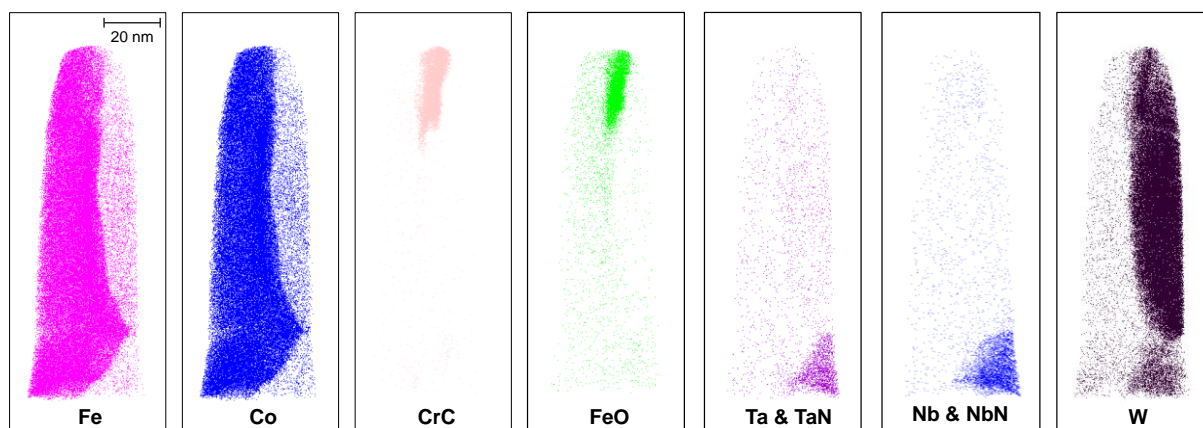
Figure 3.14: Reconstructions of an APT data set showing the same volume using different ions. This technique enables to detect precipitates and other features.

3.5.2 Particle compositions

Particle compositions were obtained by using isosurfaces. Isosurfaces are surfaces around volumes that contain a predefined concentration of chosen elements. One way to select the optimal concentration value for an isosurface is to calculate 1D concentration profiles along a cylinder as shown in figure 3.15. By doing so, the concentration of different ions inside a particle is revealed and values of isosurfaces can be found (as shown in figure 3.15 d)). Once a particle is surrounded by an isosurface, the isosurface value has to be optimized in a way that no matrix ions are included inside the isosurface, in order to obtain an accurate concentration of the particle. By using 1D concentration profiles as a function of the distance from the isosurface (cf. figure 3.16), the isosurface value is changed until the ionic concentrations inside the isosurface are constant.

After optimizing the isosurface value, a new mass spectrum was generated only for the ions inside the isosurface. The final particle compositions after decomposition of overlapping peaks are presented and discussed in section 4.2.2.
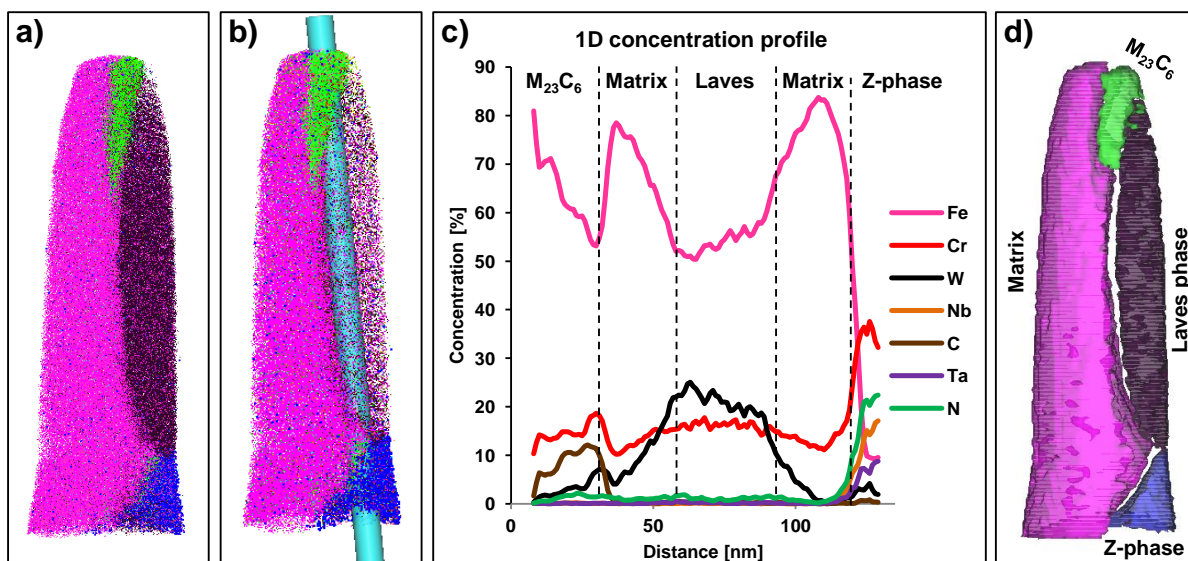
Figure 3.15: Procedures of analyzing a reconstructed APT data set: a) the reconstructed volume with all ions; b) define and place a cylinder to find the concentration of the particles; c) 1D concentration profile along the cylinder; d) four isosurfaces which divide the volume into four sub-volumes: matrix, $M_{23}C_6$, Laves phase and Z-phase.
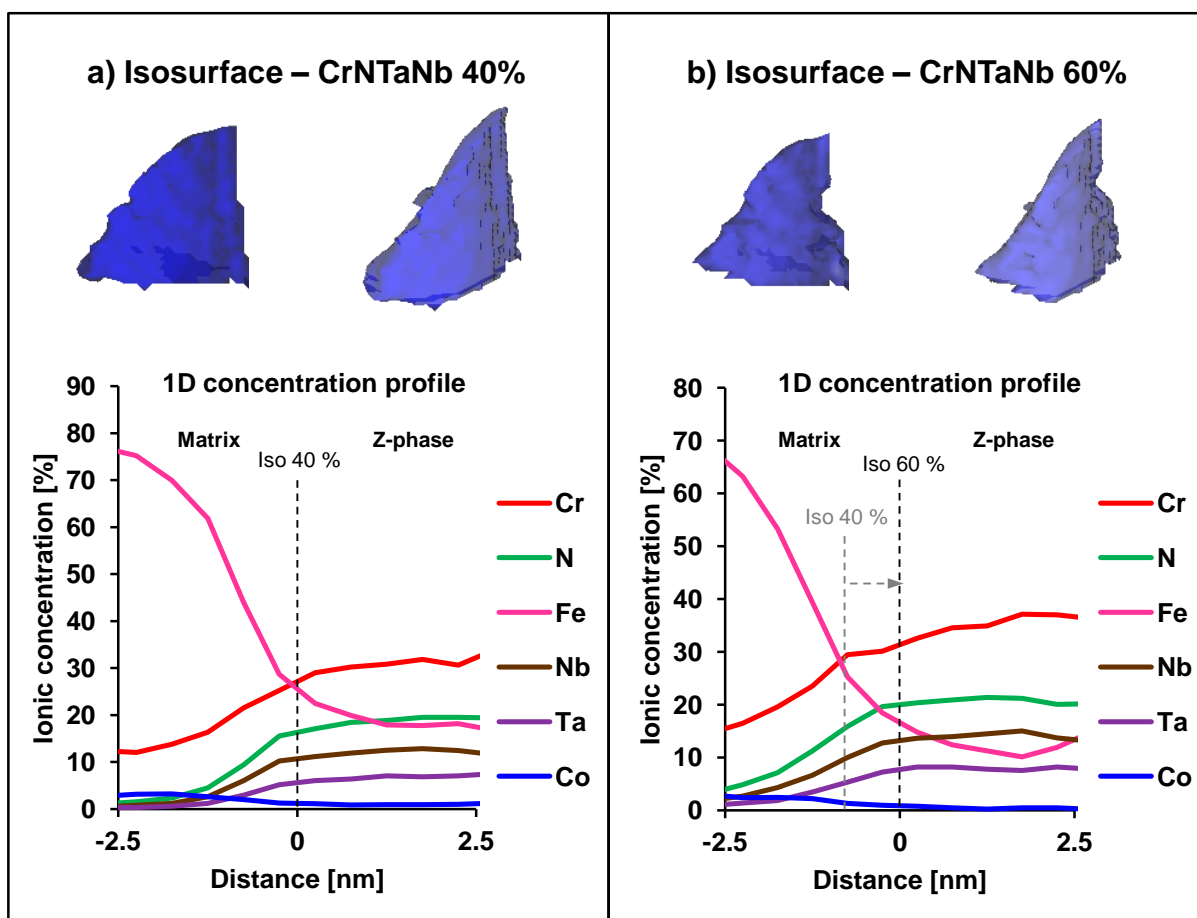
Figure 3.16: Method of optimizing the isosurface value, a Z-phase particle: a) CrNTaNb 40 %: concentrations at surface are not constant; b) CrNTaNb 60 %: constant ionic concentrations inside the extracted volume.

31

4 Results and Discussion

4.1 SEM investigations on Laves phase

Analysis of Laves phase particles was performed using a Leo Ultra 55 FEG SEM. Laves phase (Fe_2M (M = W and/or Mo)) contains much higher amounts of tungsten and molybdenum compared to the matrix of the investigated steels. Thus, Laves phase appears brighter than the matrix when backscattered electrons are used for detection. $M_{23}C_6$ particles show only low contrast to the matrix. However, MX (M = Ta and/or Nb, X = C and/or N) particles appear also very bright. Therefore, one of the important tasks was to distinguish Laves phase and MX. Figure 4.1 shows two typical micrographs that were obtained with the QBSD detector. Several precipitates have been analyzed using EDX with software *Inca 4.15*. It was found that although both types of these particles appear brighter than the matrix, the shape of the particles was different: Laves phase has an irregular shape, whereas MX particles have a circular shape. This was used to differentiate these particles.

From figure 4.1 it can also be seen that MX particles are brighter than Laves phase particles in steel ZU3, and slightly darker than Laves phase particles in steel ZU2. This result is plausible, since MX particles in steel ZU2 contain also Nb which has a lower atomic number compared to Ta. Furthermore, Laves phase in ZU3 contains also Mo that has a lower atomic number than W. A lower atomic number means that fewer electrons are backscattered and consequently a darker appearance in the micrograph.

In this section, the results of the SEM image analysis are discussed.
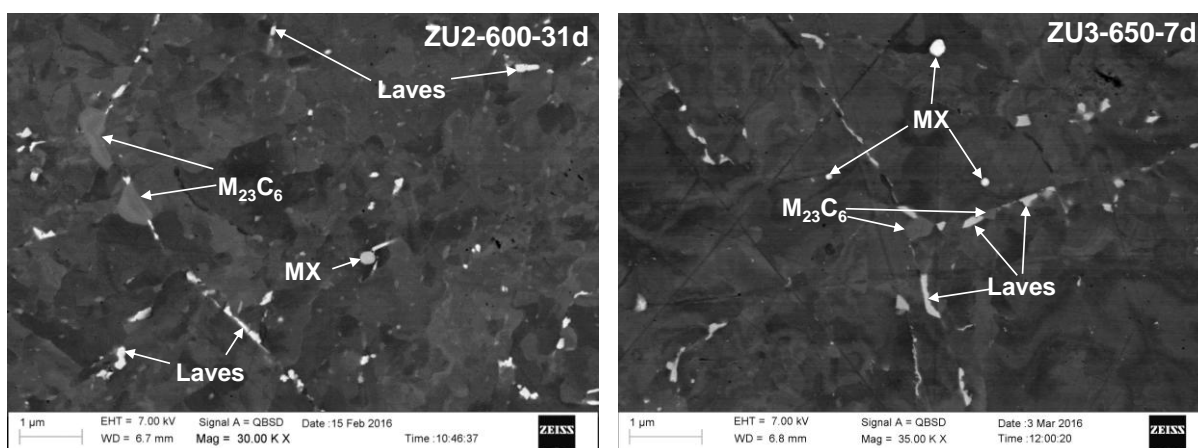
Figure 4.1: SEM BSE micrographs showing different precipitates: the alloy ZU2 aged for 31 days at 600 °C (left), and ZU3 aged for 7 days at 650 °C (right).

4.1.1 Laves phase particle sizes

Figure 4.2 shows the mean equivalent circle diameters $\bar{d}$ of Laves phase particles as a function of aging time for steels ZU2 and ZU3 aged at 600 °C (blue), 650 °C (green) and 700 °C (red). Error bars are 95 % confidence intervals calculated after reference [51]:

$$\Delta d = \pm t \cdot \frac{s}{\sqrt{n}} , \qquad [14]$$

where t is a multiplier that depends on the number of images per image sequence (e.g. $t = 2.064$ for 25 images) and s is the standard deviation for all n particles:

$$s = \left[\frac{\sum_{i=1}^{n} (d_i - \bar{d})^2}{n - 1} \right]^{1/2} \qquad [15]$$
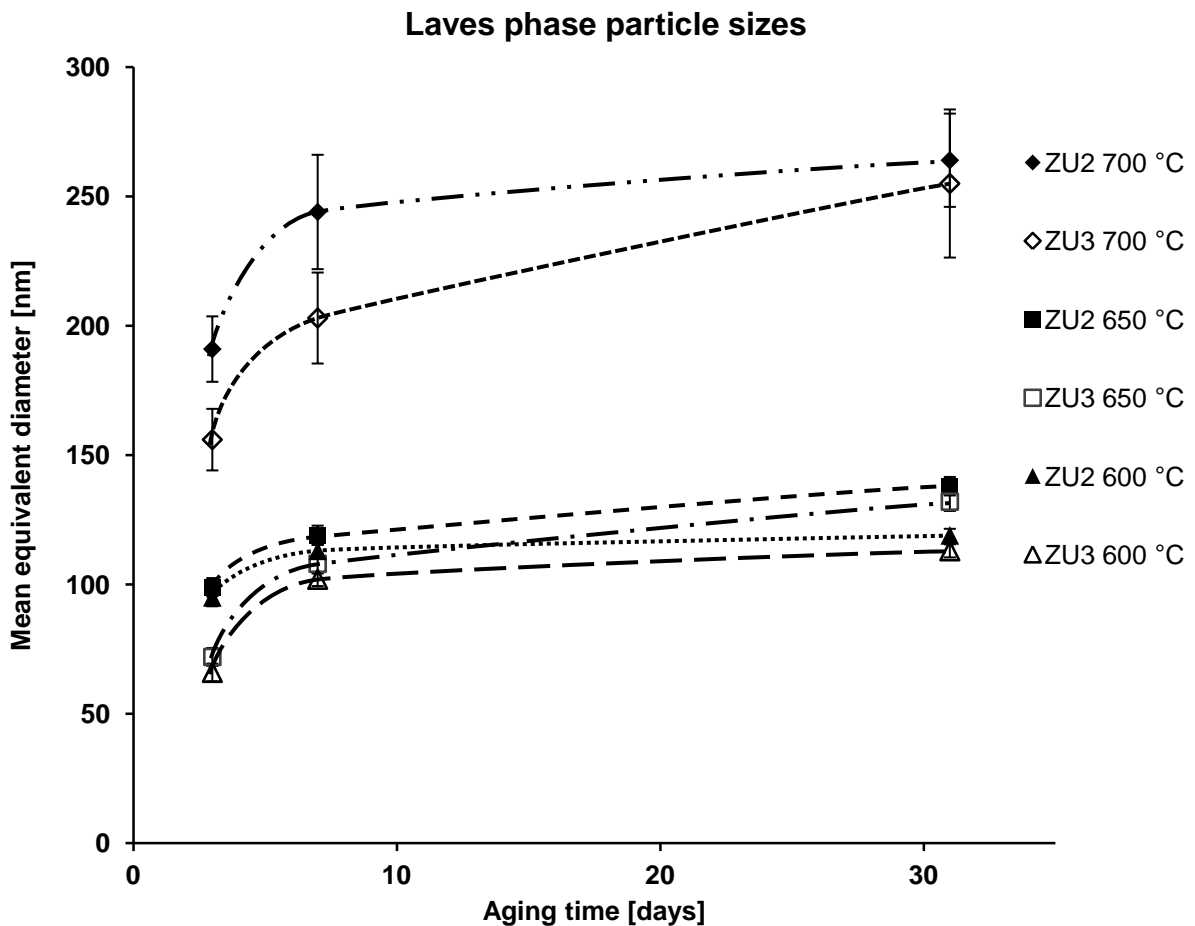
Figure 4.2: Mean equivalent circle diameters with 95 % confidence intervals of steels ZU2 and ZU3 versus aging time. Dashed lines were drawn to guide the eyes, indicating trends of particle size evolution during aging.

In all specimens, there is a fast increase in Laves phase size between 3 and 7 days. After 7 days, Laves phase size in the specimens aged at 600 °C stays nearly constant, whereas at higher temperatures the average diameters still increase. In general, measured particle sizes are larger with higher aging temperature. Especially at 700 °C, Laves phase is very coarse. The reason behind this is that at higher temperatures the driving force for nucleation of Laves phase is lower and thus, fewer nuclei are formed. Furthermore, at higher temperatures the diffusion process inside the material is faster. As a result, fewer particles are formed which grow faster.

Laves phase particles analyzed in steel ZU3 are found to be slightly smaller compared to Laves phase in steel ZU2: 119 nm, 138 nm and 264 nm (ZU2) vs. 113 nm, 132 nm and 255 nm (ZU3) after 31 days of aging at 600 °C, 650 °C and 700 °C. However, Laves phase particles show a stronger tendency to grow in ZU3 in the early stages of aging, and may become even larger compared to Laves phase in ZU2 after longer times of aging.

Figure 4.3 shows a comparison of equivalent diameters in steel ZU3 measured in this work with those published by Dimmler et al. [52]. Dimmler used the same analysis technique that was applied in this work. He investigated steel NF616 (P92) that contains the same amounts of W and Mo but has a lower amount of Cr, which has negligible influence on the precipitation behavior of Laves phase. Unfortunately, no published data for the same aging times could be found. However, the graph shows that measured particle sizes in both works are comparable and follow a similar trend.

Laves phase particle sizes - ZU3
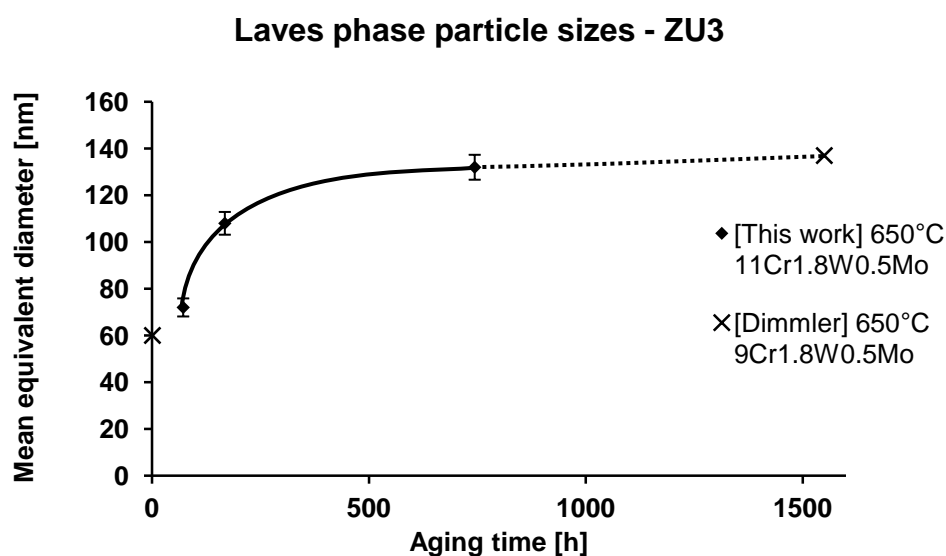
Figure 4.3: Comparison of mean equivalent diameters of steel ZU3 with equivalent diameters measured by Dimmler et al. [52] for steel P92. Lines were drawn to guide the eyes.

In figure 4.4, histograms showing Laves phase size distributions of steels ZU2 and ZU3 aged at 650 °C for 3, 7 and 31 days are compared. Calculated mean diameters are indicated by red bars in the diagrams. Furthermore, the number of particles and number density of Laves phase obtained from each sequence is included to the histograms. The number densities will be discussed in section 4.1.3.

Both steels have in common that the tail of the particle size distribution shifts to larger particle diameters for longer aging times, which is due to the effects of particle growth and Ostwald ripening. Once particles are nucleated, they begin to grow. Since nucleation continues until the equilibrium solute concentration is reached, particles that have nucleated earlier, have longer times to grow and thus, shift the tail to longer aging times. When Laves phase is fully precipitated, these particles start to coarsen due to Ostwald ripening [53].

Histograms for Laves phase size distributions after aging at 600 °C and 700 °C can be found in the appendix (appendix 1 and 2) of this work. They show the same behavior as obtained in figure 4.4.

The histograms obtained at 650 °C and 700 °C indicate that Ostwald ripening starts between 7 days and 31 days of aging, since the shape of the distribution changes and gets a more bimodal character. Small Laves phase particles get consumed by bigger particles, which could explain the formation of a "second peak" after longer aging times. This peak is not observed in the histograms after aging at 600 °C.

Another result can be obtained from the shape of the distributions: the particle size distributions in steel ZU2 are broader than the distributions in steel ZU3, which show a very sharp peak at smallest Laves phase particle sizes. A reason might be that Laves phase is different distributed in these steels. In steel ZU2, Laves phase precipitates mostly at Cu particles, whereas in steel ZU3 more $M_{23}C_6$ particles will serve as nucleation sites, because of the high C content.

In figure 4.5, the histograms after 31 days of aging are compared as a function of the aging temperature. This comparison yields an elongated tail of the particle size distribution for increased aging temperatures. Higher temperatures increase diffusion and particles will grow faster until the equilibrium solute concentration is achieved. Therefore, fewer particles have time to nucleate and coarsening will start earlier [53].
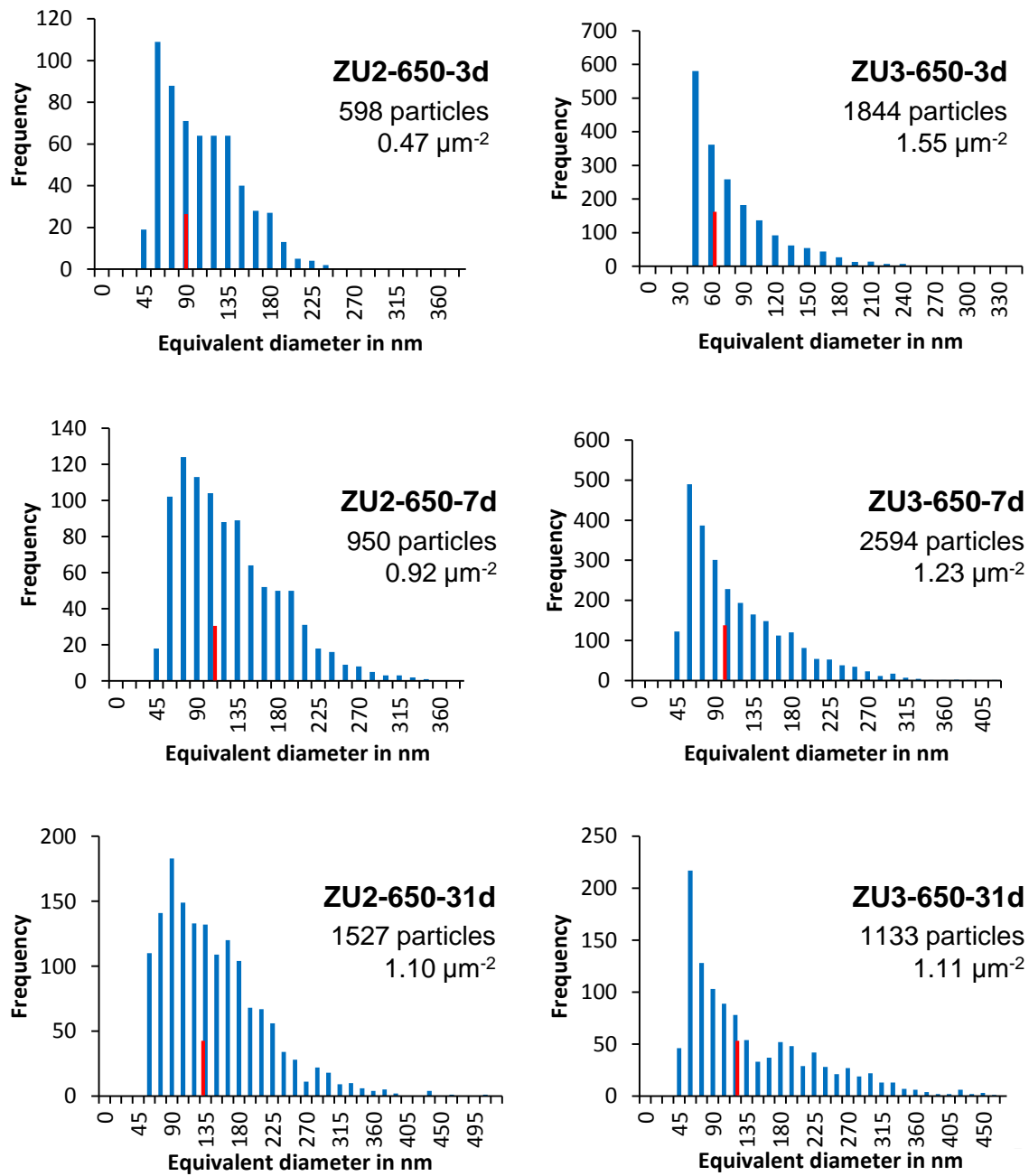
Figure 4.4: Histograms showing Laves phase size distributions for steels ZU2 (left) and ZU3 (right) aged at 650 °C for 3 (top), 7 (middle) and 31 days (bottom), red bars indicate mean equiv. diameters.
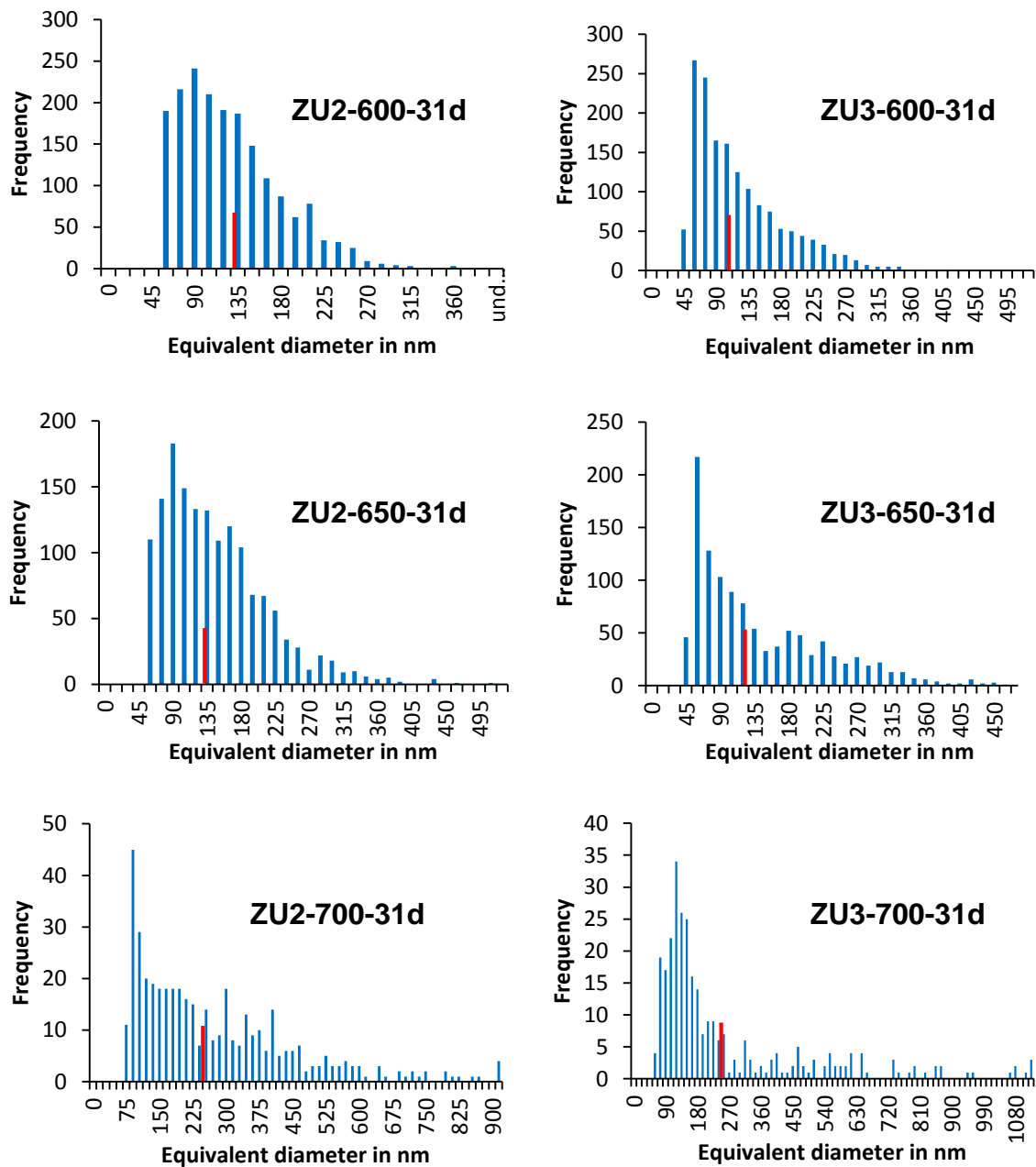
Figure 4.5: Histograms showing Laves phase size distributions for steels ZU2 (left) and ZU3 (right) aged for 31 days at 600 °C (top), 650 °C (middle) and 700 °C (bottom), red bars indicate mean equiv. diameters.

4.1.2 Laves phase area fractions

In figure 4.6, area fractions determined by image analysis (cf. section 3.3) are plotted as a function of aging time. The area fraction is proportional to the volume fraction of Laves phase. The amount of Laves phase was found to be higher in steel ZU3. This result is plausible since steel ZU3 contains more Laves phase forming elements (0.56 at% W + 0.3 at% Mo) compared to steel ZU2 (0.64 at% W). The amount of Laves phase is similar after 31 days of aging at 600 °C and 650 °C in each steel, but it is significantly lower after aging at 700 °C. The reason is that Mo and W have higher solubilities in the α-iron matrix at higher temperatures. The evolution of area fractions shows a strong increase within the first 7 days of aging and seems to converge to a plateau at longer aging times indicating the end of the particle growth state. The area fraction after 7 days of aging for steel ZU3 aged at 700 °C seems to be too low compared with the other data points which could have been affected by an inhomogeneous particle distribution.
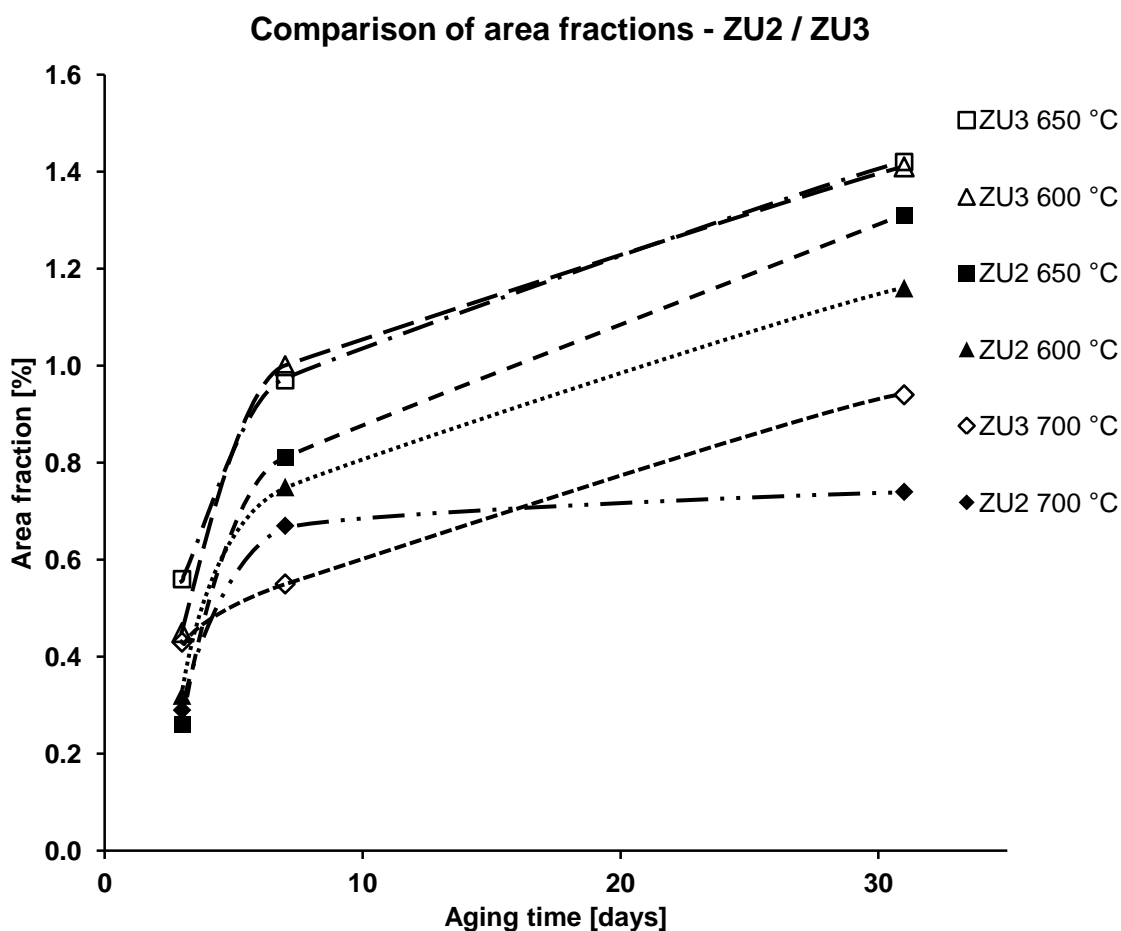
Figure 4.6: Area fraction of Laves phase in steels ZU2 and ZU3 versus aging time. Continuous lines mark trends of area fraction evolution. Dashed lines were drawn to guide the eyes, indicating trends of area fraction evolution during aging.

In order to calculate the molar equilibrium fractions of Laves phase at different temperatures (cf. table 2 and figure 4.7), simulations with *JMatPro* using the database for general steel and with *ThermoCalc* using the database TCFE6 were performed. The simulations confirm that the amount of Laves phase is higher in steel ZU3. Since Laves phase and the *α*-iron matrix have different densities, molar and area/volume fractions cannot be directly compared. Assuming, that the composition of Laves phase is exactly Fe_2W and the amount of other phases (e.g. $M_{23}C_6$) is negligibly, the molar fractions $X_{M,Laves}$ can be converted into area/volume fractions $X_{V,Laves}$. The lattice parameter of *α*-iron a_{Fe} is 2.867 Å. The lattice parameters of hexagonal (C14 type of structure) Laves phase are 4.737 Å (a_{Laves}) and 7.694 Å (c_{Laves}) [54].

$$X_{M,Laves} = \frac{n_{Laves}}{n_{Laves} + n_{Fe}}$$

$$\Leftrightarrow n_{Fe} = n_{Laves} \cdot \frac{(1 - X_{M,Laves})}{X_{M,Laves}} \quad [16]$$

and

$$X_{V,Laves} = \frac{V_{Laves}}{V_{Laves} + V_{Fe}} = \frac{n_{Laves} \cdot V_{atomic,Laves}}{n_{Laves} \cdot V_{atomic,Laves} + n_{Fe} \cdot V_{atomic,Fe}} \quad [17]$$

where V_i is the volume of a phase, $V_{atomic,i}$ is the volume per atom in the elementary cell and n_i the number of atoms referring to phase i, with:

$$V_{atomic,Laves} = \frac{a_{Laves}^2 \cdot c_{Laves} \cdot \sin(60°)}{12} \text{ and } V_{atomic,Fe} = \frac{a_{Fe}^3}{2} \quad [18]$$

Combining equations [17] and [18], the area/volume fraction $X_{V,Laves}$ is calculated by:

$$X_{V,Laves} = \frac{V_{atomic,Laves}}{V_{atomic,Laves} + \frac{(1 - X_{M,Laves})}{X_{M,Laves}} \cdot V_{atomic,Fe}} \quad [19]$$

The simulated molar fractions converted into area fractions are also listed in table 2.

Table 2: Laves phase fractions determined by SEM image analysis (area) after 31 days of aging at different temperatures compared with calculated equilibrium fractions (molar) and converted into area fractions (area*) obtained by *JMatPro* and *ThermoCalc.*

Temperature [°C]	Phase fraction in ZU2 [%]			Phase fraction in ZU3 [%]		
	SEM [area]	*JMatPro* [molar | area*]	*ThermoCalc* [molar | area*]	SEM [areal]	*JMatPro* [molar | area*]	*ThermoCalc* [molar | area*]
600	1.16	1.49 | 1.57	1.39 | 1.47	1.41	1.70 | 1.80	1.54 | 1.63
650	1.31	1.24 | 1.31	1.12 | 1.18	1.42	1.41 | 1.49	1.26 | 1.33
700	0.74	0.85 | 0.90	0.71 | 0.75	0.94	0.98 | 1.04	0.85 | 0.90

Comparison with JMatPro
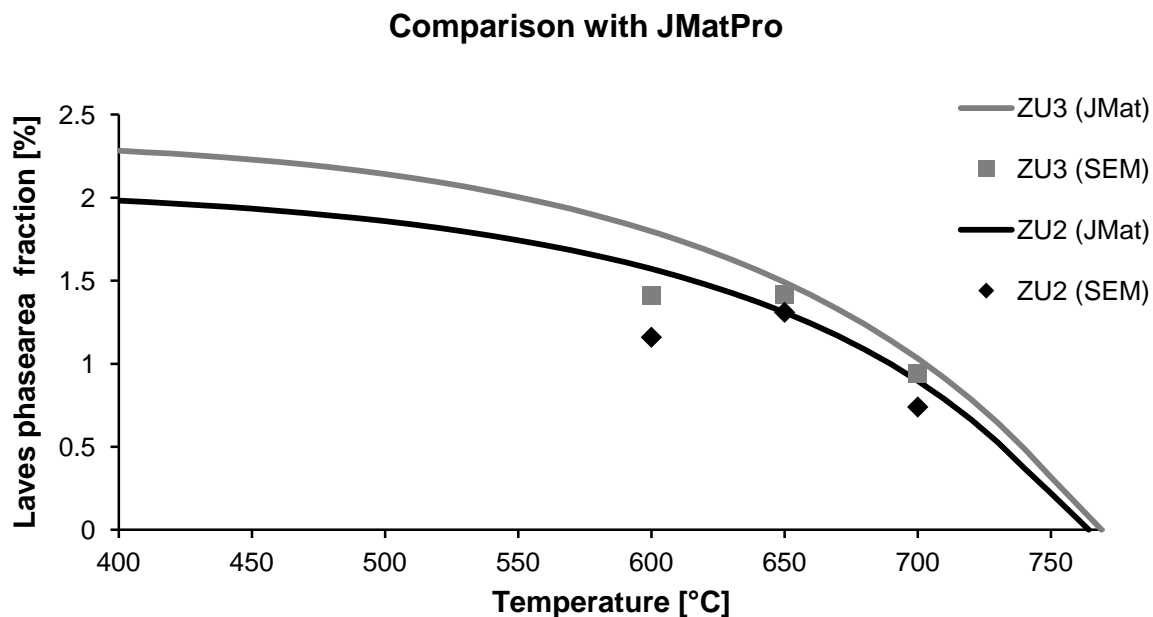
Figure 4.7: Comparison of measured and simulated area fractions of Laves phase as a function of temperature in steels ZU2 and ZU3. Simulations performed with *JMatPro* (general steel database).

The direct comparison of measured and simulated area fractions of Laves phase reveals that the equilibrium state is not reached after 31 days of aging at 600 °C, since the simulated fractions are slightly larger. After aging at 650 °C and 700 °C, the amount of Laves phase nearly corresponds to the calculated equilibrium amounts. This indicates that nucleation and growth of Laves phase is faster at 650 °C and 700 °C and is finished within the first 1000 h of aging, whereas at 600 °C a longer time for nucleation and growth is expected. More exact statements would require more experimental data of specimens after even longer aging, which are not available yet. Nevertheless, this result is in good agreement with time-temperature-precipitation analysis via X-ray diffraction of Mimura et al. [55] and quantitative evaluations of Dimmler et al. [52] performed on steel NF616 (P92), which is comparable to steel ZU3.

The facts that *JMatPro* and *ThermoCalc* use different databases and that no Ta was available for the simulations in *ThermoCalc,* explain the differences in the simulated equilibrium fractions. It is worth noticing that the conversion of molar into volume fractions was based on many assumptions and is not exact. For example, the change in the crystallography of Laves phase due to the addition of Mo was ignored. Furthermore, the graphical analysis of area fractions is prone to measurement errors. It is also influenced by inhomogeneous particle distributions, which can cause deviations (cf. section 4.1.4).

4.1.3 Laves phase number densities

Figure 4.8 shows the comparison of Laves phase number densities in steels ZU2 and ZU3 after aging for different times and temperatures. Since Laves phase particles were not distributed homogeneously and not all SEM images were taken with the same magnification, the values for number densities are not as accurate as the particle diameters and area fractions (cf. section 4.1.4 for accuracy of measurement results). A higher magnification means that smaller Laves phase particles can be detected, which increases the number density value. The black arrows in figure 4.8 indicate where the measured data points are expected, if the same magnification would have been used for all SEM images. Nevertheless, several conclusions can be drawn from the evaluation of number densities. The higher the temperature, the lower is the observed number density. This behavior is reasonable since, the closer the aging temperature to the solution temperature of Laves phase is (cf. figure 4.7), the more difficult it is for Laves phase to nucleate. At 700 °C, only a few particles nucleate, and they grow much faster (compare with particle diameters).
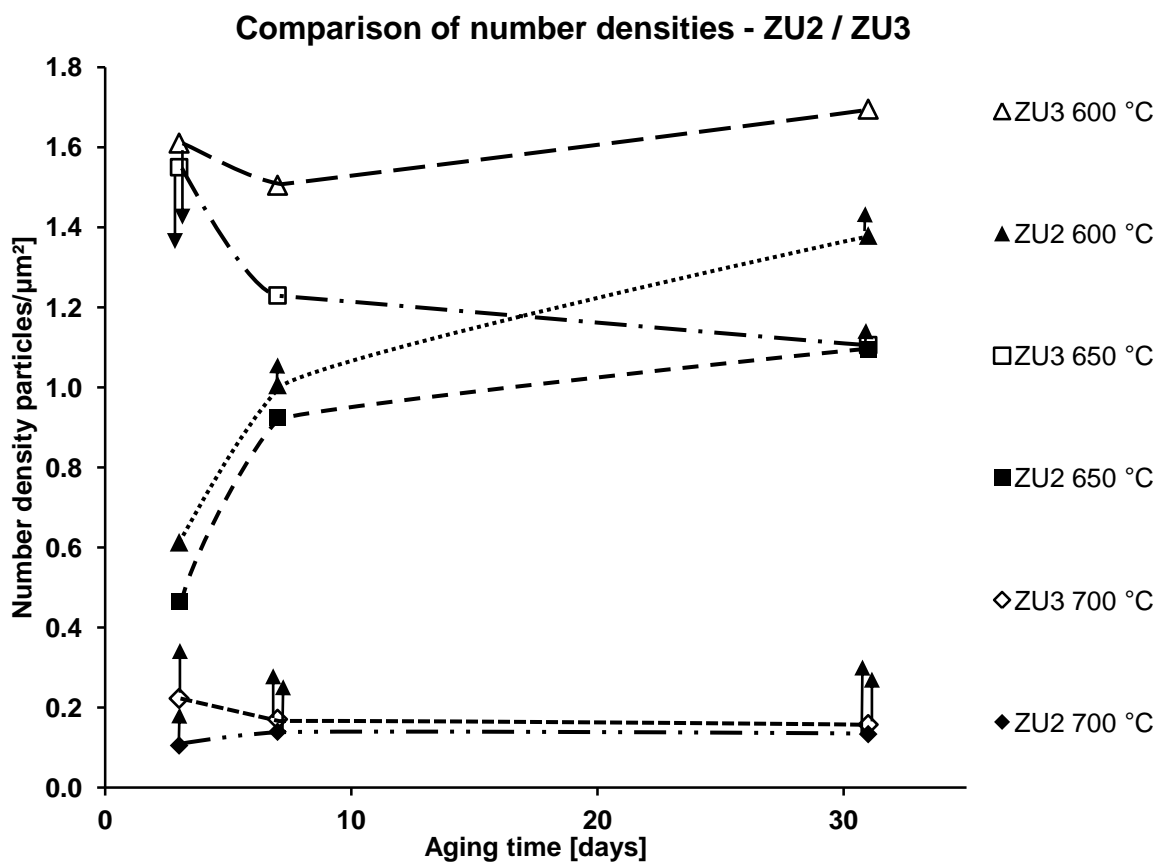
Figure 4.8: Number density of Laves phase in steel ZU2 and ZU3 versus aging time. Dashed lines were drawn to guide the eyes indicating the trend of number density evolution. Arrows indicate in which direction data points would get shifted, if the same magnification for SEM images would always have been used.

41

The number densities after 3 and 7 days of aging are larger in steel ZU3. A possible explanation is the higher amount of Laves phase in steel ZU3 at heat treatment temperature of 750 °C (cf. figure 4.7). Thus, more Laves phase is already formed during heat treatment.

All curves in figure 4.8 converge to a plateau. No significant decrease in number densities is observed after 7 days of aging, which would indicate that Laves phase did not start to coarsen before 31 days of aging, in contrast to the results obtained from the histograms after aging at 650 °C and 700 °C. A possible explanation for this difference is that the particle number densities reach their maximum between 7 and 31 days of aging. Another reason could be that the decrease in number densities due to coarsening is smaller than the measurement error for the analysis of Laves phase number densities and thus could not be observed. Also in this case, investigation of specimens after longer aging times is needed.

4.1.4   Accuracy of measurement results

As already mentioned in previous sections, a quantitative image analysis is prone to measurement errors. In order to estimate the reproducibility of the measurement results, two image sequences were taken at different locations on the specimen. The comparison of the results is shown in table 3. The first specimen (ZU2 aged at 700 °C for 3 days) was investigated with two different magnifications. Both analyses yielded very similar results. The second specimen was steel ZU3 aged for 3 days at 650 °C. This analysis shows comparable equivalent diameters, whereas the area fractions and especially the number densities are deviating. The good agreement in particle diameters justifies the small error bars in figure 4.2 and confirms the quality of the measured particle sizes with this analysis technique.

The deviations in area fractions and particle number densities are caused by measurement errors and by inhomogenities in particle distributions. The SEM analysis has shown that especially for the specimens aged for short times, some areas on the specimens contain more precipitates than other parts. Since the magnification was very high (50000x), and thus the total investigated area smaller, these inhomogenities have a large influence on the area fraction and number density. High magnifications have only been used for specimens of steel ZU3 aged for 3 days at 600 °C and 650 °C. The expected error in area fractions and number densities for the other specimens is lower. Furthermore, steel ZU3 showed continuous layers of Laves phase along grain boundaries. These layers lead to problems during image analysis, since they were cut into many small particles by using the watershed algorithm (cf. figure 4.9). In the shown analysis, this made a difference of around 250 particles in the complete sequence. The results depend strongly on the amount of grain boundaries in the investigated area. The continuous layers of Laves phase have mainly been observed for the 3 days aged specimens (600 °C and 650 °C) of steel ZU3. Thus, real Laves phase number densities are expected to be slightly lower than the measured ones in figure 4.8.

Measurement errors are introduced by setting the threshold value and the manual removal of MX particles. It is possible that some MX particles were included in the Laves phase analysis, since EDX analysis could not be performed for all particles. MX particles have been removed by looking at the shape of the particles only. Nonetheless, the measurement errors seem to be small because of the good match of measured data with equilibrium calculations and also with the data obtained by Dimmler et al. [52].

Table 3: Reproducibility of measurement results: Two image sequences of steel ZU2 aged for 700 °C for 3 days and steel ZU3 aged at 650 °C for 3 days have been taken for comparison. Each column is split into the results of the 1. and 2. analysis.

Sample	Magnification [Kx]		Equivalent diameter [nm]		Area fraction [%]		Number density [particles/ µm²]	
	1.	2.	1.	2.	1.	2.	1.	2.
ZU2-700-3d	25	30	190	192	0.28	0.31	0.10	0.11
ZU3-650-3d	50	50	74	70	0.67	0.43	1.86	1.29

Original image

Threshold

Outlines after threshold

Outlines after using the watershed
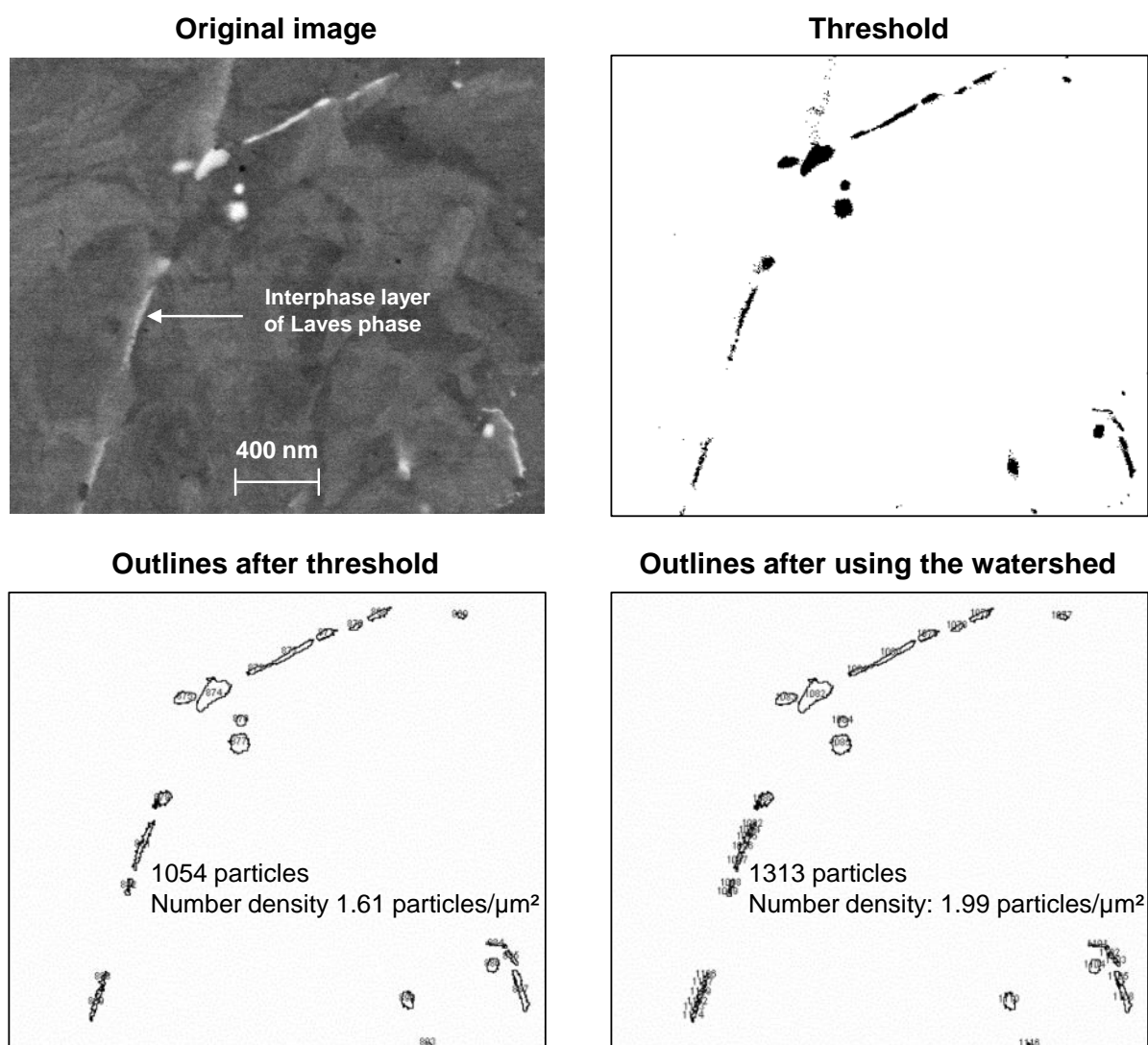
Figure 4.9: Extract of an SEM micrograph of steel ZU3 aged for 3 days at 600 °C shown at different stages during image analysis. The continuous layer of Laves phase leads to a strong increase in the number of particles when using the watershed algorithm of *ImageJ*.

4.2   Atom probe investigations

Atom probe analyses were performed with the laser and the voltage mode. Only minor differences in compositions can be found when comparing matrix compositions obtained by laser and by voltage mode (cf. tables 4 and 5). The greatest difference is found in the amount of Si ions. The reason is that Si migrates on the tip's surface and appears more densely distributed at the laser incident side of the specimen. This is a typical artifact of laser assisted atom probe measurement and is often found in literature (cf. figures 4.10 c) + d) and references [43] and [56]).
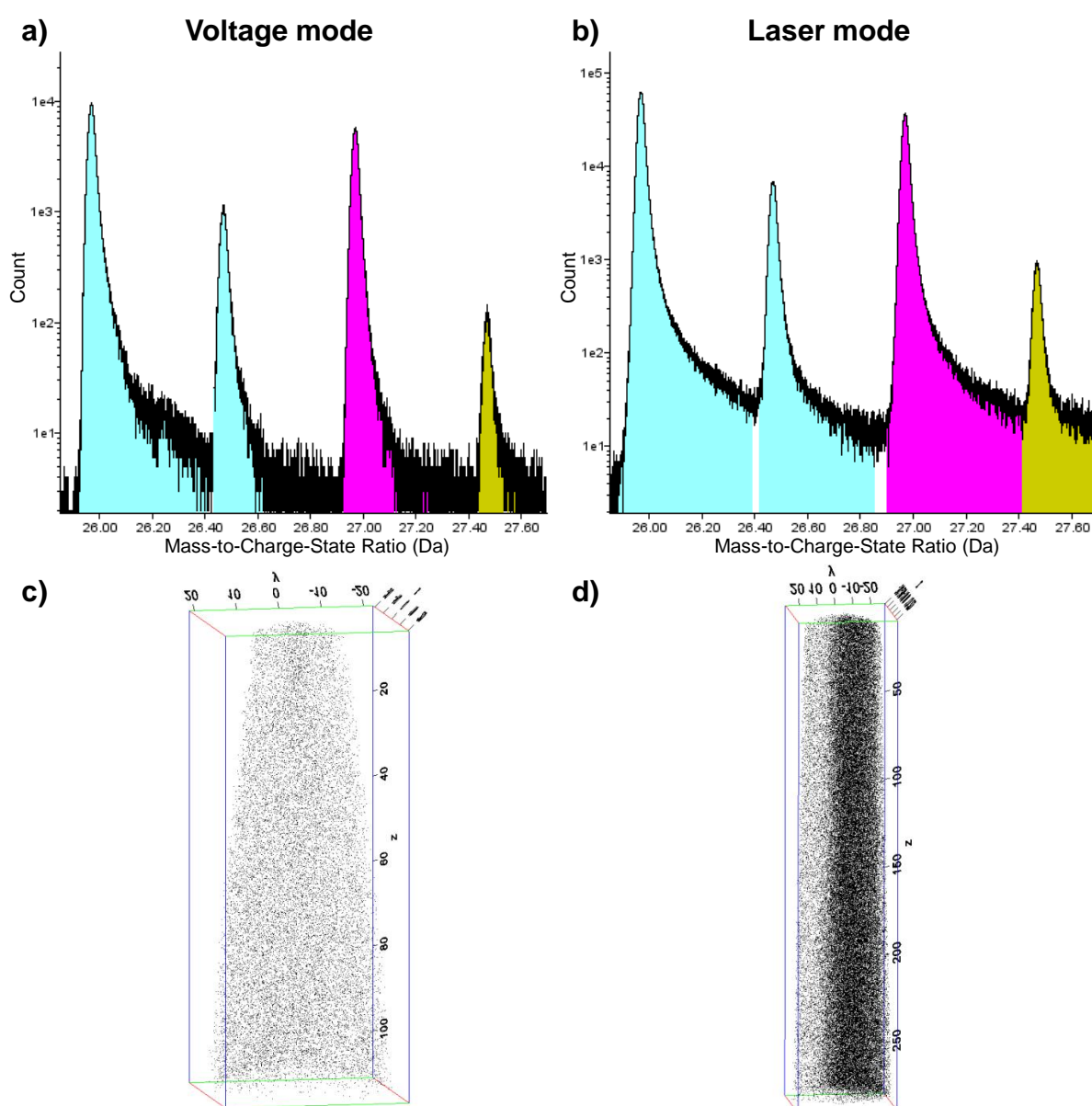
Figure 4.10: Comparison of APT data sets obtained by voltage (left column) and by laser mode (right column): figures a) and b) show mass spectra; figures c) and d) show the distribution of Si ions.

Another artifact of laser assisted atom probe measurement is that peaks in the mass spectrum are more unsymmetrical compared to those obtained by voltage mode (cf. figures 4.10 a) and b)). Peaks in the laser mode show tails in the direction of higher mass-to-charge states, which, if big enough, may influence neighboring peaks. Also this effect is found in literature [43] and will not be discussed here in more detail.

Nevertheless, these artifacts do not significantly influence the measured concentrations. The most significant influence of using laser mode is on the analyzed volume of the specimen. Specimens analyzed with the voltage mode fractured in average after ~4 million detected ions; compared to a fracture after ~30 million ions with the laser mode. The small data sets obtained with the voltage mode drastically decreased the probability of obtaining particles. All the particles analyzed in this work are obtained with the laser mode.

Another interesting result was found when comparing the stability of steels ZU2 and ZU3 against premature fracture under voltage pulsing. The number of evaporated ions in steel ZU2 until specimen fracture was around three times as large as in steel ZU3. An explanation for this behavior could not be found and requires further studies.

4.2.1 Evolution of the matrix

Tables 4 and 5 show matrix compositions of steels ZU2 and ZU3 after 31 days of aging obtained by APT in comparison with data obtained by equilibrium calculations with *JMatPro*. Every listed concentration is the average of 1-4 (mostly 2-3) APT measurements. The concentrations of Si, Co, Mn and Ni are constant over aging time and close to the as manufactured ones, since these elements do not form precipitates. The concentrations of N, C, B, Nb, and Ta are close to zero, indicating that most of these atoms already formed precipitates. Some minor deviations might be due to measurement close to a particle which increased the measured concentration. B segregates at grain boundaries; thus, there is no B found in the matrix. The concentrations of Fe and Cr vary a little between the different aging temperatures, but there is no clear trend, as can be seen in the equilibrium data. Trends can be found when comparing the concentration of W, Mo, and Cu. Therefore, below only the changes in the concentrations of W and Cu in steel ZU2 and of W and Mo in steel ZU3 are further compared and discussed. Since W and Mo mainly precipitate as Laves phase, the concentrations of W and Mo left in the matrix have to be inverse to the amount of Laves phase and thus, enable a comparison between APT and SEM results.

Table 4: Matrix concentrations (at%) of steel ZU2 obtained by APT (by laser and voltage pulsing) in comparison with equilibrium calculations of *JMatPro* after aging for 31 days at different temperatures. The last column shows the concentration of ZU2 after vacuum induction melting.

Elements in steel ZU2	600 °C			650 °C			700 °C			after VIM
	laser	voltage	JMatPro	laser	voltage	JMatPro	laser	voltage	JMatPro	
Fe	83.579	83.601	83.814	83.897	84.074	83.608	83.312	84.673	83.309	80.95
Cr	11.898	11.849	11.738	11.866	11.365	11.773	12.116	10.512	11.801	12.11
Co	2.983	3.107	3.173	2.929	3.119	3.158	2.985	3.098	3.139	3.05
Si	0.661	0.622	0.663	0.541	0.629	0.661	0.506	0.667	0.659	0.64
W	**0.269**	**0.242**	**0.141**	**0.199**	**0.236**	**0.222**	**0.342**	**0.334**	**0.351**	**0.64**
Ni	0.201	0.217	0.168	0.175	0.227	0.167	0.173	0.228	0.167	0.16
Cu	**0.159**	**0.148**	**0.174**	**0.204**	**0.186**	**0.278**	**0.420**	**0.313**	**0.441**	**1.82**
Mn	0.144	0.120	0.130	0.147	0.116	0.131	0.128	0.111	0.132	0.13
N	0.005	0.065	0.000	0.003	0.026	0.000	0.001	0.033	0.000	0.17
C	0.000	0.014	0.000	0.007	0.008	0.000	0.002	0.014	0.000	0.14
Nb	0.002	0.005	0.000	0.002	0.007	0.000	0.001	0.008	0.000	0.10
Ta	0.008	0.001	0.000	0.009	0.000	0.000	0.003	0.001	0.000	0.06
B	0.001	0.002	0.000	0.001	0.001	0.000	0.000	0.000	0.000	0.03
O	0.088	0.010	-	0.022	0.008	-	0.014	0.009	-	-

Table 5: Matrix concentrations (at%) of steel ZU3 obtained by APT (by laser and voltage pulsing) in comparison with equilibrium calculations of *JMatPro* after aging for 31 days at different temperatures. The last column shows the concentration of ZU3 after vacuum induction melting.

Elements in steel ZU3	600 °C			650 °C			700 °C			after VIM
	laser	voltage	JMatPro	laser	voltage	JMatPro	laser	voltage	JMatPro	
Fe	84.553	85.162	84.760	84.295	84.387	84.614	84.207	84.703	84.423	82.60
Cr	11.429	10.518	11.221	11.489	11.305	11.270	11.456	10.980	11.321	12.20
Co	2.839	3.047	3.049	2.944	3.067	3.039	2.857	2.913	3.025	3.00
Si	0.505	0.523	0.454	0.514	0.477	0.457	0.544	0.521	0.462	0.47
W	**0.175**	**0.182**	**0.115**	**0.207**	**0.174**	**0.181**	**0.270**	**0.277**	**0.286**	**0.56**
Ni	0.190	0.261	0.206	0.220	0.241	0.206	0.248	0.249	0.205	0.20
Mo	**0.140**	**0.148**	**0.074**	**0.147**	**0.146**	**0.110**	**0.217**	**0.227**	**0.157**	**0.30**
Mn	0.145	0.121	0.121	0.142	0.132	0.122	0.158	0.122	0.122	0.12
N	0.002	0.023	0.000	0.003	0.012	0.000	0.012	0.005	0.000	0.15
C	0.006	0.004	0.000	0.007	0.046	0.000	0.007	0.001	0.000	0.24
Ta	0.008	0.006	0.000	0.006	0.001	0.000	0.007	0.001	0.000	0.14
B	0.001	0.003	0.000	0.000	0.000	0.000	0.000	0.001	0.000	0.02
O	0.007	0.005	-	0.030	0.013	-	0.017	0.000	-	-

Aging at different temperatures:

In figures 4.11 (steel ZU2) and 4.12 (steel ZU3) the concentration of W and Cu/Mo in the matrix are compared with the equilibrium calculations based on *JMatPro* as a function of aging temperature after 31 days of aging. Error bars indicate the standard deviation between the different measurements.

The measured Cu concentrations in steel ZU2 follow the trend of the simulated concentrations. The measured concentrations are slightly lower (especially for 650 °C), which means that more Cu precipitated than expected from the simulation. Since the standard deviations of the measured concentrations are very small, the difference might be due to errors in the equilibrium calculations which are far from being perfect for steels that contain many alloying elements. Nonetheless, it shows that Cu reaches its equilibrium concentration before 31 days aging.

The evolution of the W concentration shows the same behavior in steels ZU2 and ZU3. At 600 °C, more tungsten is dissolved in the matrix than in the equilibrium, whereas at 650 °C and 700 °C the equilibrium concentration seems to be reached (or nearly reached for steel ZU3 at 650 °C). This result corresponds to the result obtained by the SEM investigations (cf. area fractions in section 4.1.2), indicating that the nucleation and growth stage has not been completed after 31 days of aging at 600 °C.

In addition, the values obtained by APT measurement agree well with the SEM area fractions (cf. table 2). For steel ZU2, the area fraction is highest at 650 °C, slightly lower at 600 °C and lowest at 700 °C. For steel ZU3, the measured area fractions are the same at 600 °C and 650 °C and lowest at 700 °C. The same behavior (within the scope of the measurement errors) is obtained from the ionic concentrations of W and W+Mo in the matrix for the steels, when assuming that the residual W (and Mo) atoms are precipitated as Laves phase (compare with figure 4.7).

Compared to W in ZU3, Mo in ZU3 does not reach the simulated equilibrium concentrations. The measured concentrations of Mo in the matrix are around 0.05 % larger for all aging temperatures. This could be either due to a systematic error in the simulation or due to a slower diffusion of Mo into Laves phase. A slower diffusion of Mo could be proved by measuring steels with longer aging times and comparing if the Mo concentration stays constant. An error in the calculation could be proved by comparing the measured composition of Laves phase with the simulated one. The simulation might calculate a wrong ratio of W to Mo. Unfortunately, no Laves phase was obtained in the atom probe investigations of steel ZU3 in this work.
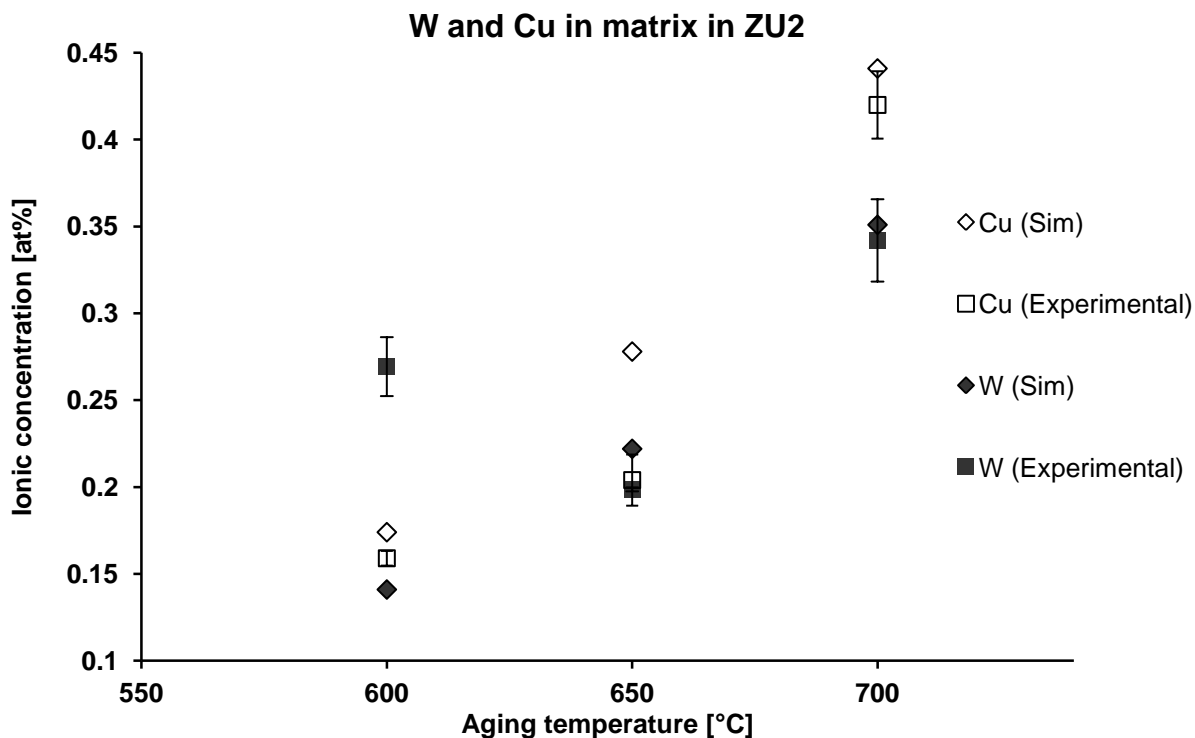
Figure 4.11: Measured and simulated concentrations of W and Cu in steel ZU2 as a function of aging temperature after 31 days of aging. Error bars are obtained via standard deviations.
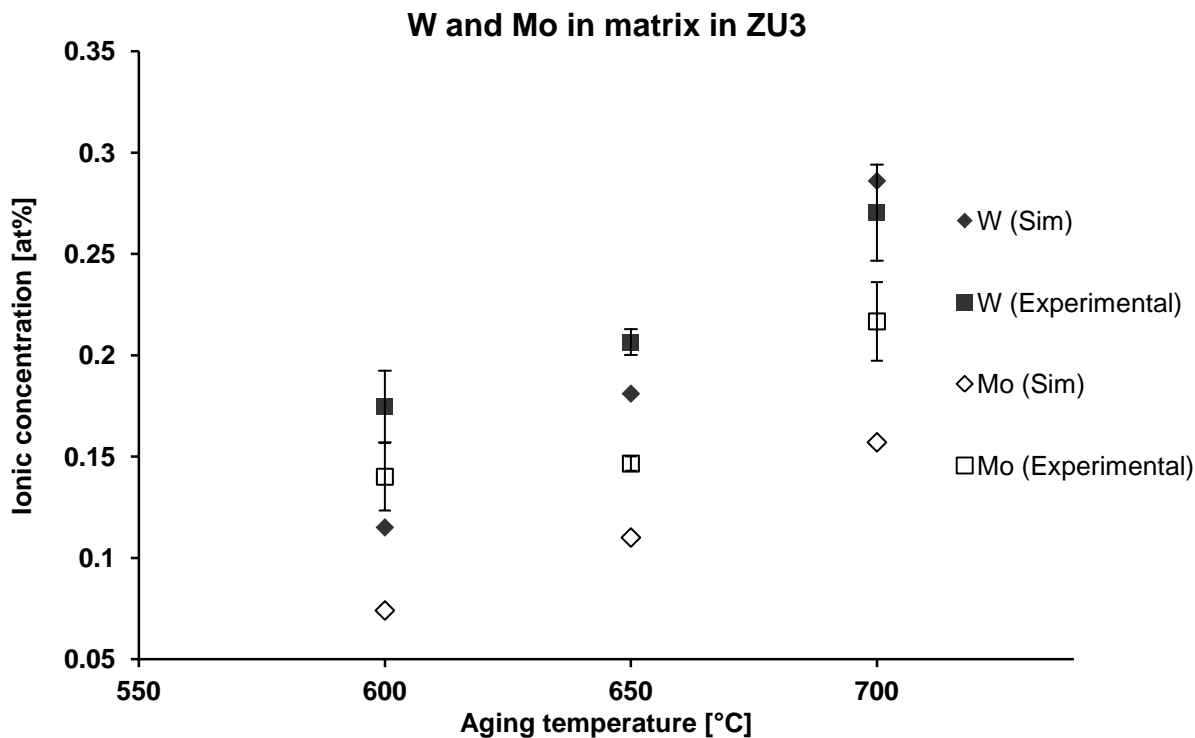
Figure 4.12: Measured and simulated concentrations of W and Mo in steel ZU3 as a function of aging temperature after 31 days of aging. Error bars are obtained via standard deviations.

Influence of aging time:

In figures 4.13 and 4.14 the concentrations of W and Cu/Mo in the matrix are compared with the equilibrium calculations based on *JMatPro* as a function of aging time after aging at 650 °C. The atom probe raw data for the steels after 0 days and 9 days of aging were performed by PhD student Masoud Rashidi. The analysis of these data was part of this work. Further, equilibrium concentrations were calculated for the matrix at tempering temperature (750 °C). These data are plotted as 0 days of aging.

The measured concentrations of W and Cu in figure 4.13 of the as tempered steel are lower than the simulated equilibrium concentrations for 750 °C. This result is plausible since the steels were heat treated for two steps at two different temperatures (4 hours at 650 °C and then 2 hours at 750 °C). Laves phase and Cu particles form already during the first step of the heat treatment. The second step of the heat treatment is too short to dissolve the precipitates again according to their equilibrium concentrations. The measured Mo concentrations in steel ZU3 (cf. figure 4.14) are higher than that calculated by *JMatPro*. Even in the as tempered condition the concentration of Mo in the matrix is higher than the equilibrium concentration for 750 °C. This deviation was also seen in figure 4.12. A possible reason for it is the same: either Mo precipitates slowly and the equilibrium has not yet been reached, or the equilibrium concentrations calculated by *JMatPro* are too low.

The evolution of the matrix concentrations of W and Cu in steel ZU2 during aging shows that the equilibrium concentrations are already reached after 9 days. It is worth noticing that all reconstructed APT data sets obtained for steel ZU2 after 9 days of aging contained particles. These might, to some extent, have influenced the measured matrix concentrations. Thus, it is difficult to draw a conclusion about how fast the precipitation of W and Cu really was. The concentration of W in steel ZU3 (cf. figure 4.14) shows the same behavior compared to steel ZU2. In the as tempered steel, more tungsten is precipitated than in the equilibrium at 750 °C. After 9 days of aging, most of the W atoms (according to the equilibrium state at 650 °C) are precipitated. Unlike steel ZU2, the equilibrium state seems not to be completely reached after 31 days of aging.

In contrast to the SEM results that showed increasing area fractions until 31 days of aging for all temperatures (cf. figure 4.6), the APT results reveal that the growth state is almost ended after 9 days of aging at 650 °C and 700 °C. A possible reason for this difference is that W and Mo accumulate first at grain/lath boundaries and thus, are removed from the matrix but cannot be detected as a particle with the SEM.
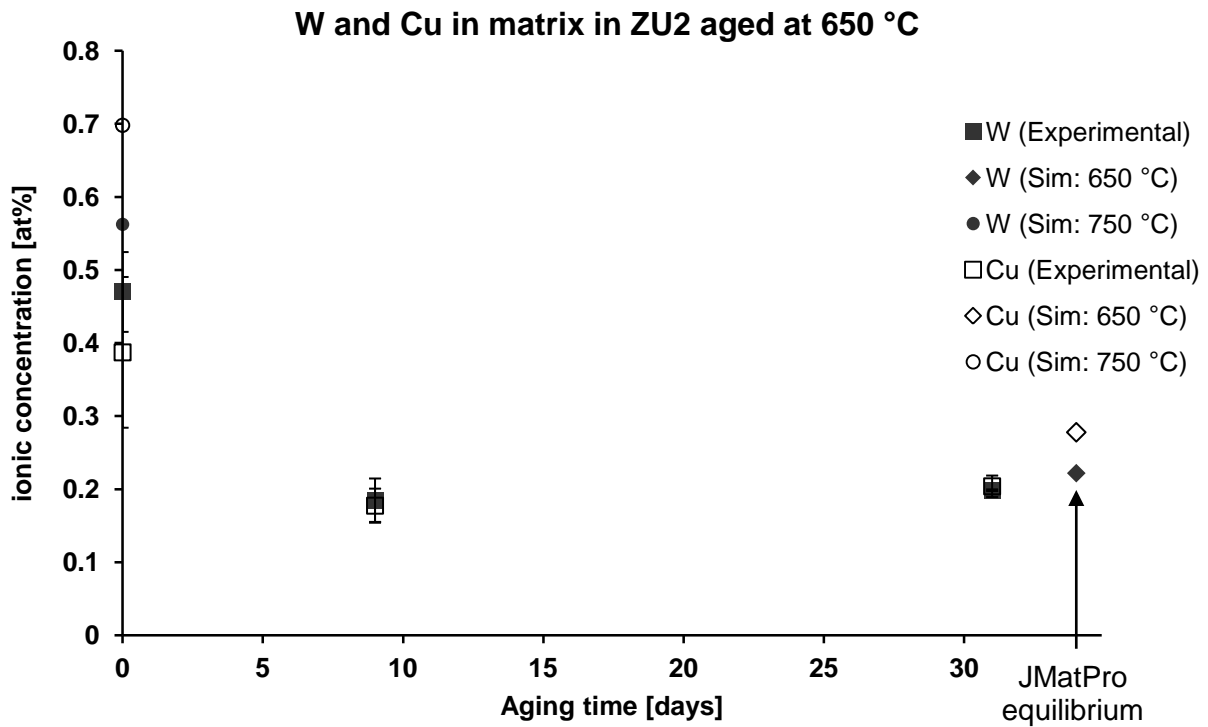
Figure 4.13: Measured and simulated concentrations of W and Cu in steel ZU2 as a function of aging time after at 650 °C. Error bars are obtained via standard deviations.
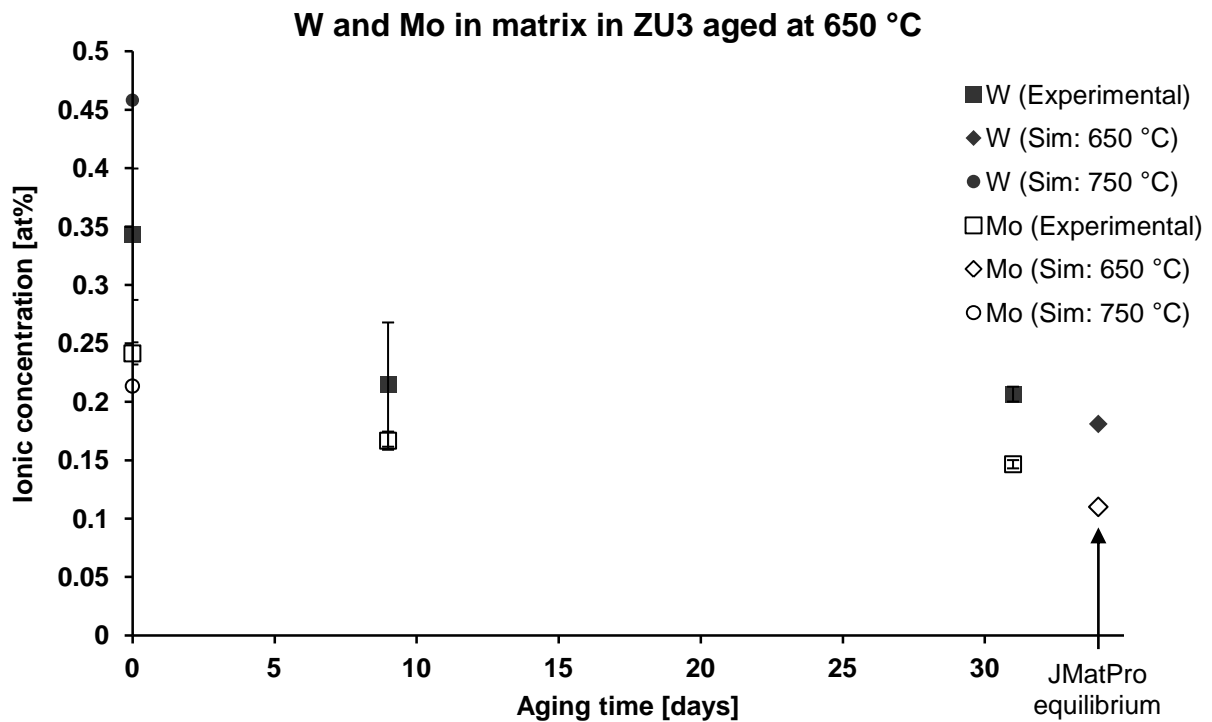
Figure 4.14: Measured and simulated concentrations of W and Mo in steel ZU3 as a function of aging time after at 650 °C. Error bars are obtained via standard deviations.

4.2.2 Evolution of particles

Various particles (Cu, $M_{23}C_6$, Laves phase, chromium nitrides, carbides, carbo-nitrides and Z-phase) have been obtained in the APT data sets. In this work, only the compositions of Laves phase, carbonitrides and Z-phase particles were analyzed and will be further discussed below.

Laves phase in ZU2:

Laves phase was only obtained in APT measurement of steel ZU2. In figure 4.15, the measured concentrations of the main constituents in Laves phase at 600 °C and 650 °C are compared with simulated data obtained by *ThermoCalc* and *JMatPro*. The error bars are the standard deviations between the Laves phase compositions measured at 650 °C. The same error bars are applied for 600° C, since only one Laves phase particle was obtained in the 600 °C measurement.

The simulated Laves phase compositions are very similar. Only the Cr content in the *ThermoCalc* simulation is slightly higher. A reason could be that no Ta is available in the database used for *ThermoCalc*. Ta is one of the Z-phase formers and thus, might have an influence on the Cr concentration in Laves phase.
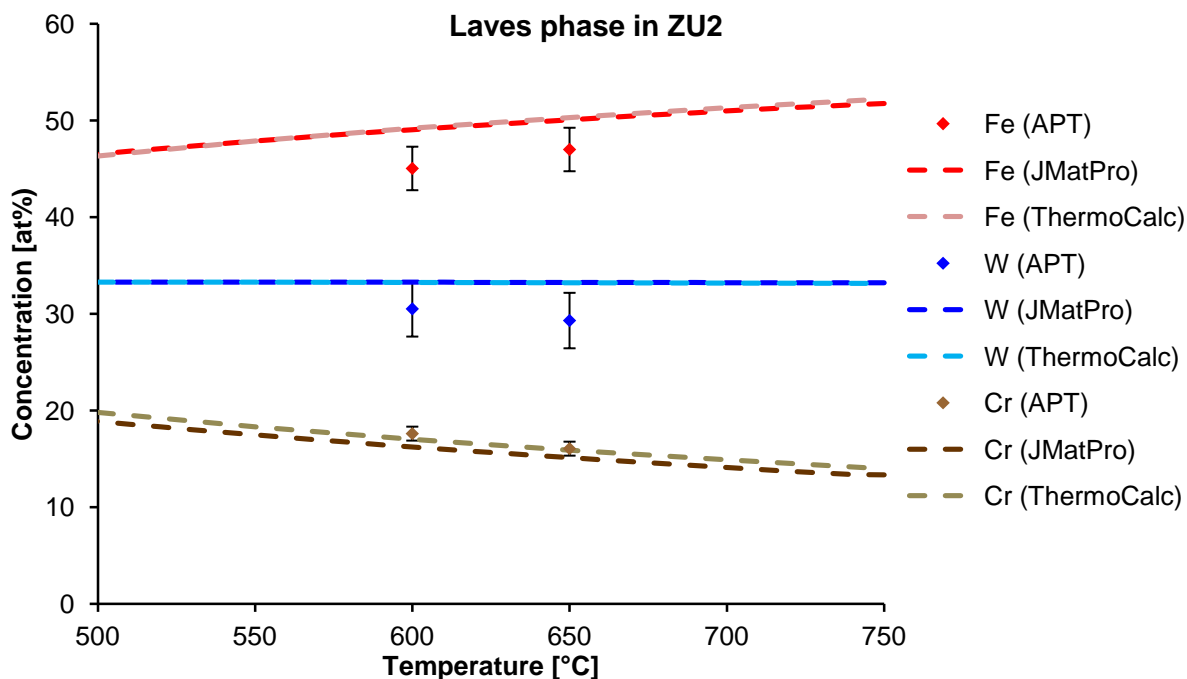
Figure 4.15: Measured concentrations of main constituents of Laves phase in steel ZU2 as a function of temperature compared with equilibrium data obtained by *JMatPro* and *ThermoCalc.*

Table 6: Concentration of constituents of Laves phase in at% obtained by APT analysis and equilibrium simulation with *JMatPro* for 600 °C and 650 °C.

Constituents of Laves phase	600 °C		650 °C	
	APT	JMatPro	APT	JMatPro
Fe	45.0	49.043	47.0 ± 2.2	50.069
Cr	17.6	16.705	16.0 ± 0.7	15.541
Co	1.7	0.377	1.8 ± 0.1	0.488
Si	2.7	0.478	3.0 ± 0.1	0.525
W	30.5	33.256	29.3 ± 2.9	33.238
N	1.1	0.000	0.9 ± 1.4	0.000
Others	1.3	0.141	1.8 ± 1.4	0.139

The main difference between simulation and measurement is found in the concentrations of W and Fe. These elements show higher concentrations in the simulations. The reason is that higher amounts of other elements are obtained in Laves phase in the measured APT data sets (cf. table 6). In the case of the presence of higher N contents, the reason might be the influence of carbonitride particles close to the Laves phase (both types of particles co-exist in the same measurement).

The differences in concentrations of Co and Si cannot be explained by neighboring precipitates, since Co and Si are not contained in high amounts in other precipitates. The standard deviation for the concentrations of Co and Si in Laves phase is very small which means that a measurement error can be excluded. For Co it could be that the equilibrium concentration is just not reached, since the amount of Co is between the expected value and the amount of Co in the matrix (~ 3 %). This explanation cannot explain the high amount of Si, since there is more Si found in Laves phase than in the matrix. Also in previous works by other authors, Si was found to have a solubility of several atomic percent in Laves phase (cf. references [5], [57] and [58]). Thus, the calculated amount of Si must be too low and the correct data should be integrated into the databases "TCFE6" used by *ThermoCalc* and "General steel" used by *JMatPro*.

Carbonitrides and Z-phase in ZU2:

Besides Laves phase, MX and Z-phase particles have been studied in this work. In steel ZU2, these are the particles that contain mainly C, N, Ta and Nb, and a varying amount of Cr. Carbonitrides/Z-phase particles were obtained in the APT data sets of the as tempered specimens, the specimens aged for 9 days at 650 °C, and for 31 days at 600 °C. No carbonitrides were found in the APT specimens aged for 31 days at 650 °C and 700 °C. It indicates that the number density of these precipitates is lower and that the precipitates are coarser, which decreases the probability to obtain any of these particles in an APT data set.

In figure 4.16 the compositions of all carbonitride and Z-phase particles detected in steel ZU2 are compared. Here the Cr content and the sum of the Nb and Ta content are plotted as a function of the C to N ratio. Error bars are estimated errors by the IVAS™ 3.6.6 software. These are statistical errors, which are smaller when the number of ions in the particle is higher.

Particles with a C to N ratio close to 0 are Z-phase particles; they contained only Cr, N, Ta and Nb. Figure 4.16 shows the clear trend that particles with lower C/N ratios contain higher amounts of Cr, whereas the amount of Ta+Nb decreases.

This trend indicates that the C content inside the carbonitrides is the limiting factor for the Z-phase transformation, since particles with higher C to N ratios have a chemical composition that is more far away from that of a Z-phase particle. It is worth noticing again that Z-phase will fully replace the carbonitrides earlier or later, as shown by thermodynamic models [26]. Z-phase that contains C has so far not been observed in any trial steel and thus, it is assumed that C has to diffuse out of the particles to be transformed to Z-phase. This seems to take more time and slows down the transformation. Atom probe tomography of steel ZU2 after longer aging times (3000 h or 10000 h) could help to verify this assumption. The amount of particles with high C/N ratios should be much lower after longer times of aging.

Another clear trend is that particles with Nb to Ta ratios larger than 1.7 contain significantly higher amounts of Cr (cf. figure 4.17). The three particles with the highest Nb to Ta ratios are already transformed to Z-phase (compare also with figure 4.16). An Nb/Ta ratio of 1.7 corresponds to the initial ratio of Nb to Ta in the matrix after VIM. These particles contained relatively high amounts of C (between 16 at% and 25 at%).

Cr- and (Ta+Nb)- concentration as a function of C/N-ratio in NbTaCN(Cr) in steel ZU2
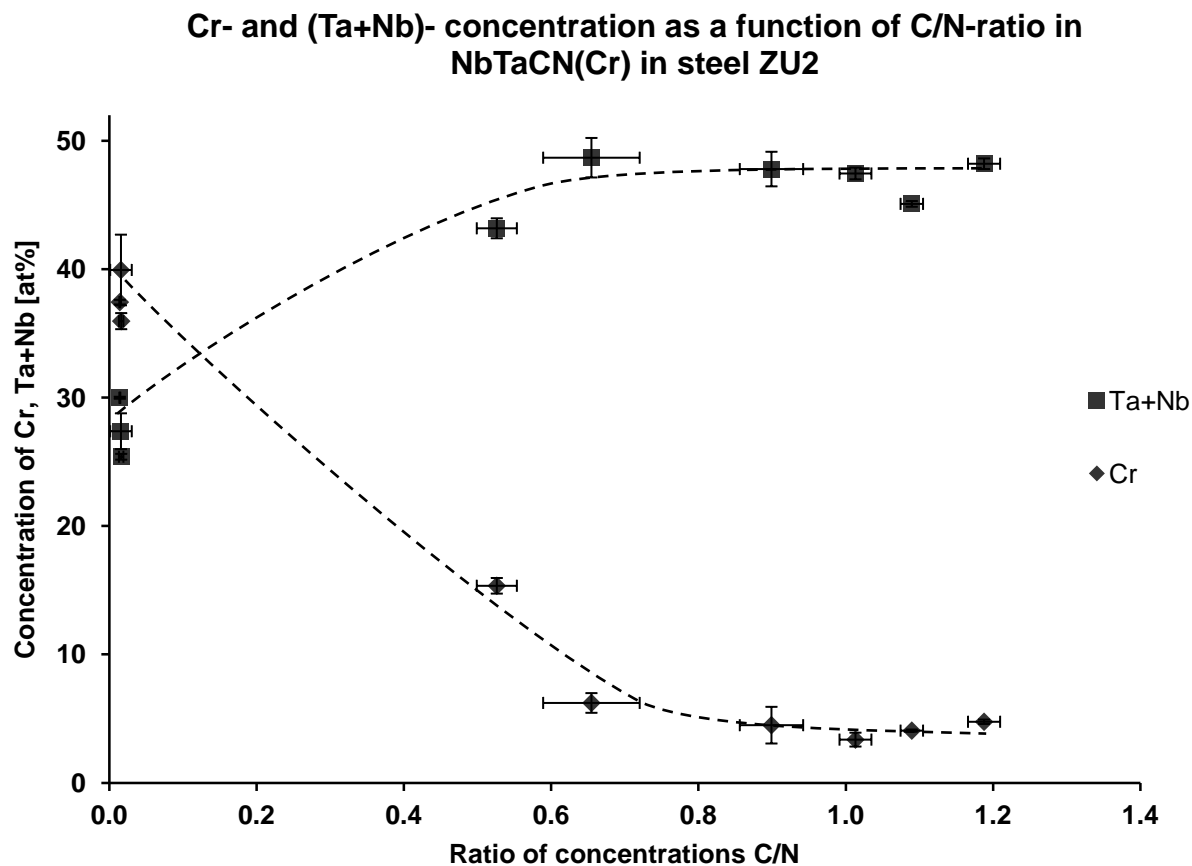
Figure 4.16: Concentrations of Cr and Ta+Nb as a function of C/N ratio in carbonitrides obtained in steel ZU2. Concentrations are in at%, error bars according to the IVAS™ software. Dashed lines were drawn to guide the eyes indicating trends in evolution of particle concentrations.

Cr as a function of Nb/Ta ratio in NbTaCN(Cr)
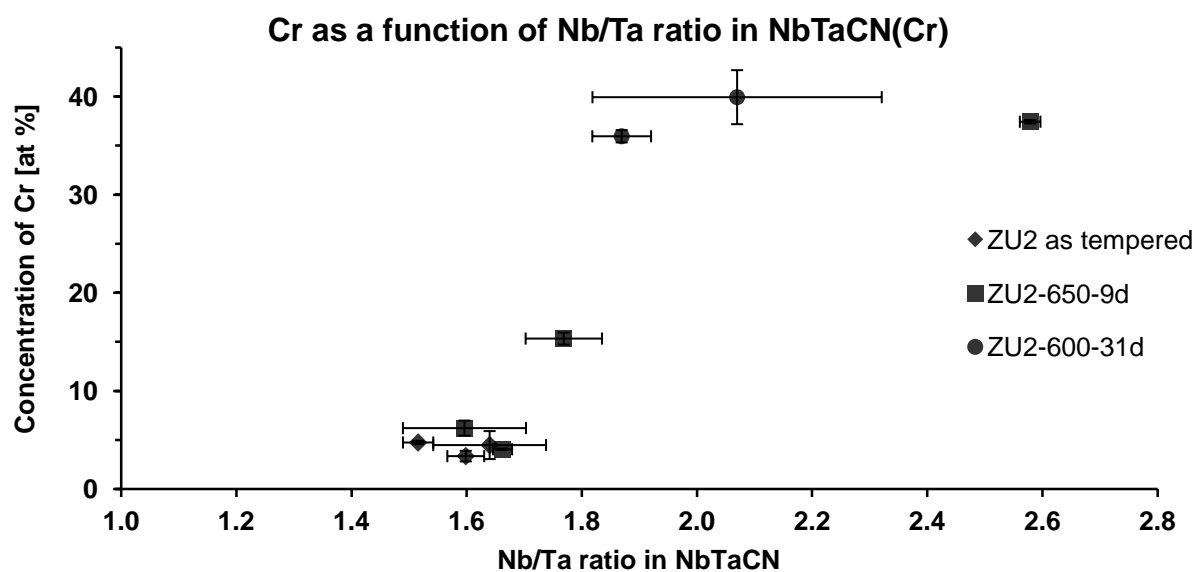
Figure 4.17: Concentration of Cr in at% as a function of the ratio of Nb to Ta atoms in carbonitrides obtained in steel ZU2. Errors are obtained from the IVAS™ software (errors for ratios via Gaussian error propagation).

From figures 4.16 and 4.17 two possible conclusions/explanations can be drawn:

1. Carbonitrides with a lower C/N ratio in the beginning (after tempering) transform faster to Z-phase and the Nb/Ta ratio increases after the transformation. A comparison of equilibrium calculations of the solubilities of Nb and Ta in MX and Z-phase particles could help to explain why the Nb/Ta ratio in Z-phase is found to be higher.

2. A high Nb to Ta ratio decreases the solubility of C in carbonitrides and thus they precipitate already with lower C contents and transform faster to Z-phase.

More atom probe measurements and equilibrium calculations are needed to clarify if the low C/N ratio or the high Nb/Ta ratio is the reason for a faster Z-phase transformation. In case of conclusion 2, carbonitrides with high Nb/Ta ratios should be found also in the as tempered specimens.

Carbonitrides in ZU3 and comparison with ZU2:

Figure 4.18 shows the Cr and the Ta concentration as a function of the C to N ratio of carbonitrides detected in the specimens of steel ZU3. The same behavior as for steel ZU2 is found: with decreasing C/N ratios, the Cr content is increasing.

No Z-phase was found in steel ZU3. A reason for this behavior is the high C content (0.24 at%) of steel ZU3 (compared to ZU2: 0.14 at%). C reduces the Cr content in the matrix and thereby decreases the driving force for Z-phase precipitation [26]. In addition, more C can partition into MX precipitates, which hinders the transformation.

The C/N ratios of carbonitrides in steel ZU3 are in general higher than the ratios found in steel ZU2 (cf. figure 4.19). A possible reason could again be the higher C content in steel ZU3.

For same C/N ratios, carbonitrides in steel ZU3 contain more Cr. Since the compositions of steels ZU2 and ZU3 are too different, this behavior cannot be explained by comparing these steels. Future investigations of a third trial steel (ZU1), which is similar to ZU2 but does not contain Nb, will help to understand, if Nb or the higher amount of C causes the higher Cr contents of carbonitrides in steel ZU3.
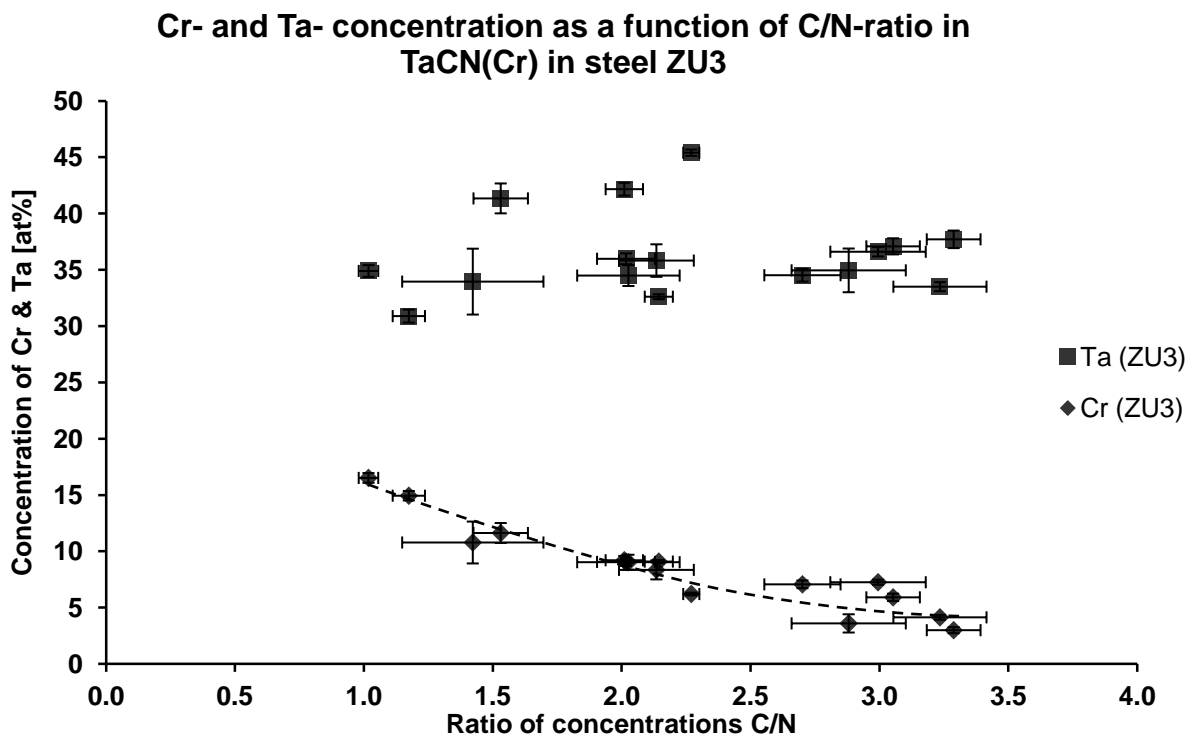
Figure 4.18: Concentrations of Cr and Ta as a function of the C/N ratio in carbonitrides obtained in steel ZU3. Concentrations are in at%, error bars according to the IVAS™ software. Dashed lines were drawn to guide the eyes indicating trends in evolution of particle concentrations.
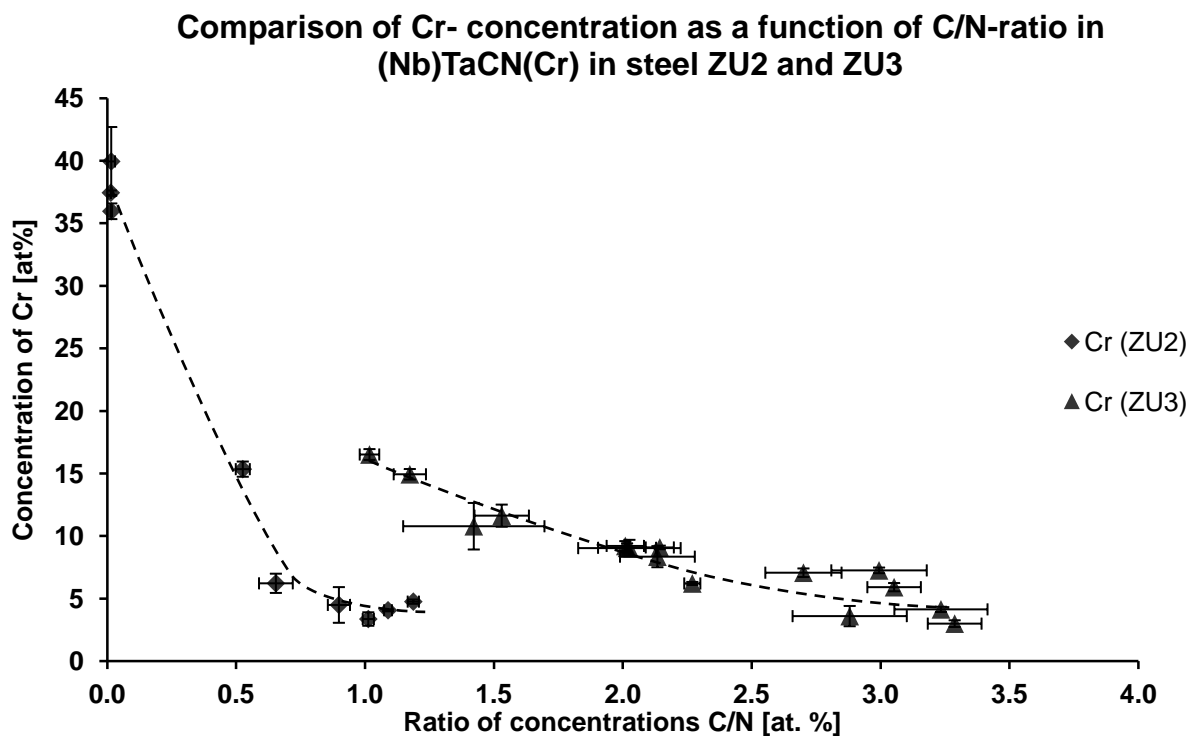
Figure 4.19: Comparison of Cr- concentrations as a function of C/N-ratio in (Nb)TaCN(Cr) particles in steel ZU2 and ZU3. Dashed lines were drawn to guide the eyes.

5 Summary

5.1 Laves phase

The evolution of Laves phase of two different trial steels during aging at 600 °C, 650 °C and 700 °C has been investigated. With a scanning electron microscope, backscattered electron image sequences of the trial steels have been taken after 3, 7 and 31 days of aging and Laves phase was identified using EDX. After post analysis with the software *ImageJ*, particle sizes, area fractions and number densities of Laves phase were obtained and compared. The comparison showed:

- Laves phase in the Mo and W containing trial steel ZU3 is smaller but shows a stronger tendency to coarsen than Laves phase in steel ZU2 that contains only W as a Laves phase forming element besides Fe.
- The amount of Laves phase was higher in steel ZU3, which could be lead back to a higher amount of Laves phase forming elements in steel ZU3.
- Laves phase number densities were slightly higher in steel ZU3 and decreased with increasing temperature according to the rules of thermodynamic.
- In contrast to steel ZU3, Laves phase in steel ZU2 does not form continuous Laves phase layers at post austenite grain boundaries. Steel ZU2 contained Cu which acts as nucleation site for Laves phase when precipitated.
- Histograms indicate a start of coarsening for both steels between 7 and 31 days of aging at 650 °C and 700 °C.

The obtained area fractions of Laves phase were further compared with equilibrium Laves phase fractions calculated with the softwares *JMatPro* and *ThermoCalc*. The comparison showed:

- The observed amount of Laves phase after 31 days of aging at 650 °C and 700 °C corresponds to the calculated equilibrium amounts in both steels and thus, it can be concluded that the particle growth state is finished.
- The thermodynamic equilibrium amount of Laves phase is not reached after 31 days of aging at 600 °C in both steels.

The concentration of W (and Mo) left in the matrix after aging was further investigated using atom probe tomography and coincided with the area fractions obtained by scanning electron microscopy. The comparison with equilibrium concentrations of W (and Mo) showed that Laves phase is already fully precipitated after 9 days of aging at 650 °C and 700 °C, but not before 31 days of aging at 600 °C for both steels.

5.2   Z-phase and carbonitrides

Z-phase and carbonitride particles in steel ZU2 (contains Nb and Ta) and steel ZU3 (contains only Ta, but more C) were characterized with atom probe tomography. The analysis of the particles' concentrations yielded:

- Particles with a low C to N ratio contain higher amounts of Cr.
- There is a direct relation between the C to N ratio and the Cr content in both steels.
- Z-phase was only found in steel ZU2. These particles showed higher Nb to Ta ratios than carbonitrides in steel ZU2.
- Carbonitrides in steel ZU3 had in general higher C to N ratios.
- Carbonitrides with the same C to N ratio contained higher amounts of Cr in steel ZU3 compared to those in steel ZU2.

6 Future work

In order to fully understand the precipitation and coarsening behavior of Laves phase in the investigated steels, studies on specimens after longer times of aging (after 3000 h and 10000 h) are required. Furthermore, the composition of Laves phase in the W and Mo containing steel ZU3 has still to be investigated with atom probe tomography.

The observed relationship between the C to N ratio and the Cr content in carbonitrides is an important piece of information that sheds more light on the precipitation process of Z-phase. Since the steels ZU2 and ZU3 are compositionally too different to draw any conclusion from a direct comparison, APT and post analysis of carbonitrides in trial steel ZU1, which is more similar to steel ZU2, have to be performed.

APT of steels that have been aged for longer times will help to understand the influence of the C content of carbonitrides on the formation to Z-phase.

Acknowledgements

I would like to express my gratitude to my examiner and supervisor assistant Professor Fang Liu for giving me the opportunity to work on a very interesting Master thesis project including the great opportunity to work with atom probe tomography.

Further, I would like to thank Professor Hans-Olof Andrén and Masoud Rashidi for their supervision and their great input to my work due to their feedback and many fruitful discussions.

I also would like to thank Professor Guido Schmitz, my examiner from the University of Stuttgart, who gave me the opportunity to come to Chalmers as an exchange student.

Further, I would like to thank Amine Yousfi, Gustav Sundell, associate Professor Mattias Thuvander and Torben Boll for their great expertise in APT and the nice discussions we had.

I also would like to thank Anders Kvist and Stefan Gustafsson for their help regarding technical issues in the lab and Cecilia Fager for answering me all my administrative related questions.

Finally, I would like to thank my family and friends for keeping my spirits up during my time in Sweden.

Appendix
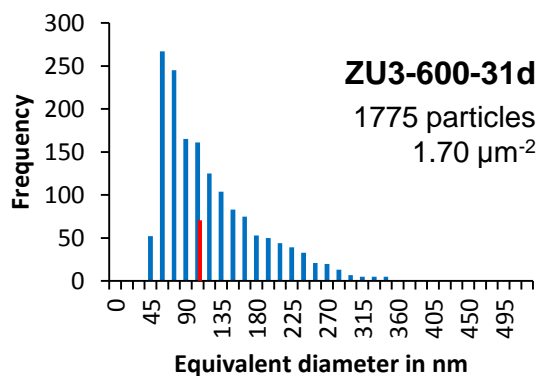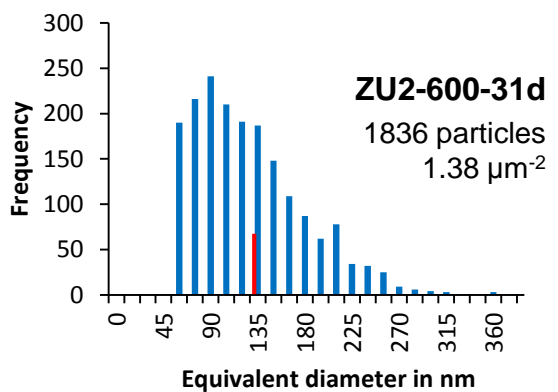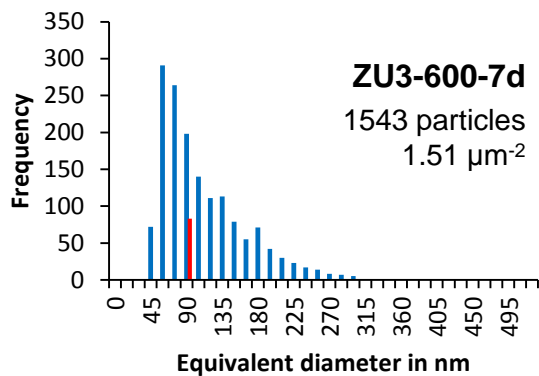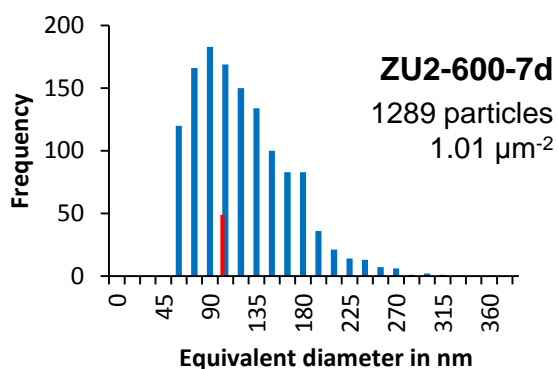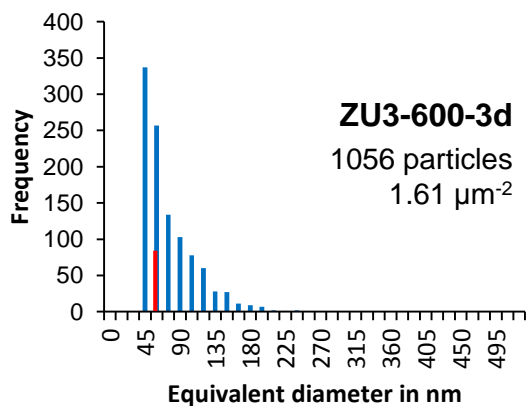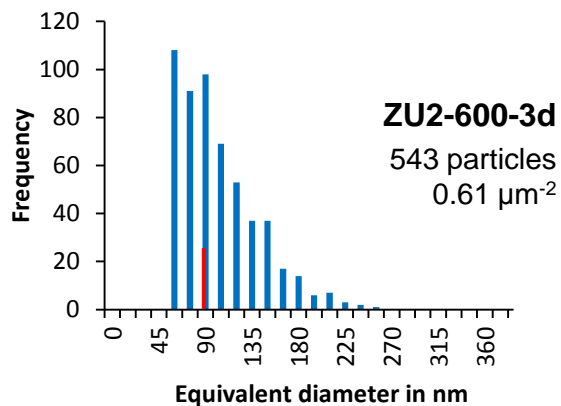
Appendix 1: Histograms showing Laves phase size distributions for steels ZU2 (left) and ZU3 (right) aged at 600 °C for 3 days (top), 7 days (middle) and 31 days (bottom).

65
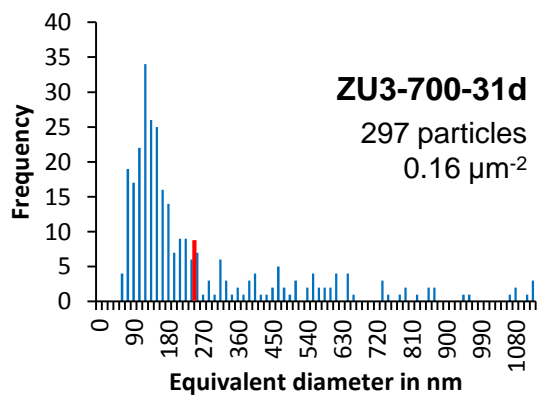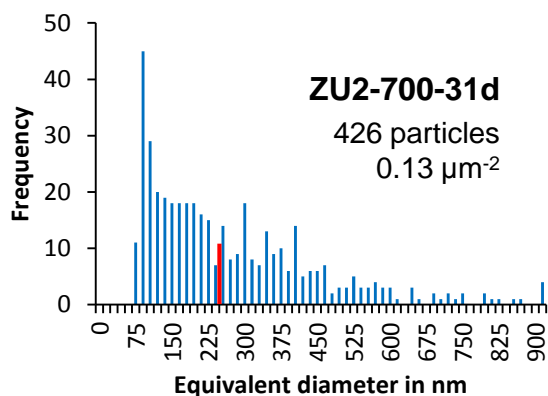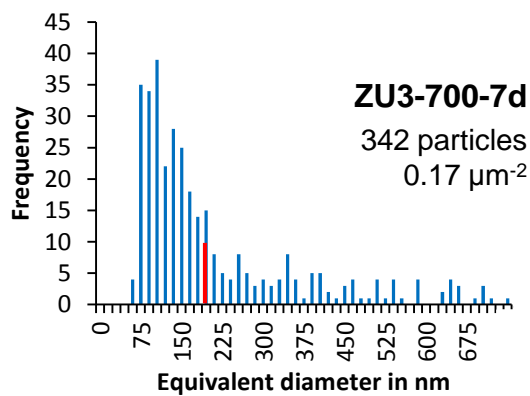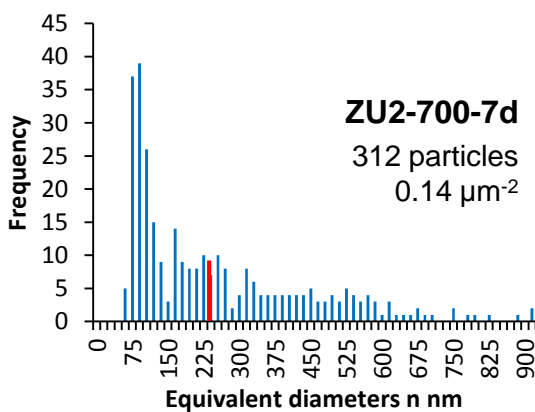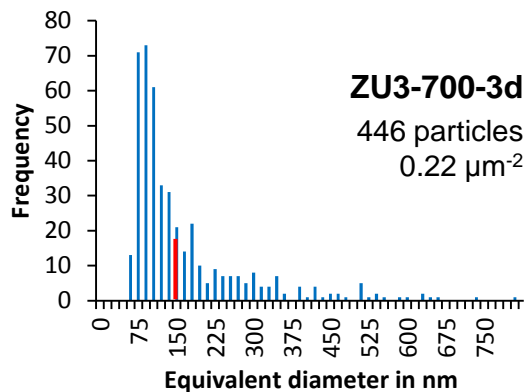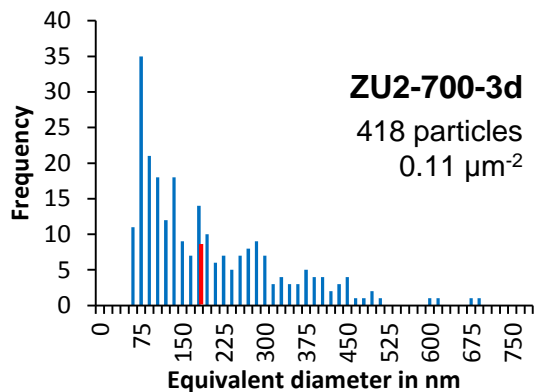
Appendix 2: Histograms showing Laves phase size distributions for steels ZU2 (left) and ZU3 (right) aged at 700 °C for 3 days (top), 7 days (middle) and 31 days (bottom).

Bibliography

[1]   Jaffee, R.I.: Metallurgical problems and opportunities in coal-fired steam power plants. *Metall. Trans. A*, **10** (2), 1979, p. 139–164.

[2]   Masuyama, F.: History of Power Plants and Progress in Heat Resistant Steels. *ISIJ Int.*, **41** (6), 2001, p. 612–625.

[3]   http://www.imoa.info/molybdenum-uses/molybdenum-grade-alloy-steels-irons/high-temperature-steel.php. *Int. Molybdenum Assoc.*, 2016.

[4]   Danielsen, H.K.: *Z-phase in 9-12% Cr Steels*. Technical University of Denmark (DTU), 2007.

[5]   Liu, F., Andrén, H.-O.: Effect of copper addition on the toughness of new Z-phase strengthened 12% chromium steels. *7th Int. Conf. Adv. Mater. Technol. Foss. Power Plants*, 2014, p. 1116–1126.

[6]   Danielsen, H.K., Hald, J.: Influence of Z-phase on Long-term Creep Stability of Martensitic 9 to 12 % Cr Steels. 2009.

[7]   Nayar, A.: *The Steel Handbook*. Tata McGraw-Hill Education, 2000.

[8]   Davis, J.R., Committee, A.S.M.I.H.: *Metals Handbook Desk Edition 2nd Edition*. Taylor & Francis, 1998.

[9]   Meyers, M.A., Chawla, K.K.: *Mechanical Behavior of Materials*. Cambridge University Press, 2009.

[10]   Pickering, F.B.: *Physical metallurgy and the design of steels*. Applied Science Publishers, 1978.

[11]   Totten, G.E. et al.: *Handbook of Mechanical Alloy Design*. Taylor & Francis, 2003.

[12]   Abe, F. et al.: Alloy design of creep resistant 9Cr steel using a dispersion of nano-sized carbonitrides. *Int. J. Press. Vessel. Pip.*, **84** (1-2), 2007, p. 3–12.

[13]   Nes, E. et al.: On the Zener drag. *Acta Metall.*, **33** (1), 1985, p. 11–22.

[14]   Ellis, R.B.: Dispersion Strengthening of metals. *Am. Sci.*, **52** (4), 1964, p. 476–487.

[15]   Ukai, S. et al.: Alloying design of oxide dispersion strengthened ferritic steel for long life FBRs core materials. *J. Nucl. Mater.*, **204**, 1993, p. 65–73.

[16]   Es-Souni, M.: Primary, secondary and anelastic creep of a high temperature near α-Ti alloy Ti6242Si. *Mater. Charact.*, **45** (2), 2000, p. 153–164.

[17]   Coble, R.L.: A Model for Boundary Diffusion Controlled Creep in Polycrystalline Materials. *J. Appl. Phys.*, **34** (6), 1963, p. 1679.

[18]   Herring, C.: Diffusional Viscosity of a Polycrystalline Solid. *J. Appl. Phys.*, **21** (5), 1950, p. 437.

[19]   Danielsen, H.K., Hald, J.: Influence of Z-phase on Long-term Creep Stability of Martensitic 9 to 12 % Cr Steels. *VGB PowerTech*, **5**, 2009, p. 68–73.

[20]   Porter, D.A. et al.: *Phase Transformations in Metals and Alloys, Third Edition*. CRC Press, 2009.

[21]   Oriani, R..: Ostwald ripening of precipitates in solid matrices. *Acta Metall.*, **12** (12), 1964, p. 1399–1409.

[22]   Taneike, M. et al.: Effect of carbon concentration on precipitation behavior of M23C6 carbides and MX carbonitrides in martensitic 9Cr steel during heat treatment. *Metall. Mater. Trans. A*, **35** (4), 2004, p. 1255–1262.

[23]   Knežević, V. et al.: Design of martensitic/ferritic heat-resistant steels for application at 650 °C with supporting thermodynamic modelling. *Mater. Sci. Eng. A*, **477** (1-2), 2008, p. 334–343.

[24]   Lee, J.S. et al.: Causes of breakdown of creep strength in 9Cr–1.8W–0.5Mo–VNb steel. *Mater. Sci. Eng. A*, **428** (1–2), 2006, p. 270–275.

[25]   Muraki, T. et al.: Creep Strengthening Mechanism of Mo and W in 9% Cr Heat Resistant Steels. *Key Eng. Mater.*, **171-174**, 2000, p. 499–504.

[26]   Danielsen, H.K., Hald, J.: A thermodynamic model of the Z-phase Cr(V, Nb)N. *Calphad Comput. Coupling Phase Diagrams Thermochem.*, **31** (4), 2007, p. 505–514.

[27]   Jack, D.H., Jack, K.H.: Structure of Z-phase, NbCrN. *J Iron Steel Inst*, **210** (Part 10), 1972, p. 790–792.

[28]   Cipolla, L. et al.: Conversion of MX nitrides to Z-phase in a martensitic 12% Cr steel. *Acta Mater.*, **58** (2), 2010, p. 669–679.

[29]   Danielsen, H.K., Hald, J.: Behaviour of Z phase in 9–12%Cr steels. *Energy Mater.*, **1** (1), 2006, p. 49–57.

[30]   Yan, W. et al.: *9-12Cr Heat-Resistant Steels*. Cham: Springer International Publishing, 2015.

[31]   Hald, J.: Long-term Stability of 9- to 12 % Cr Steels. *VGB PowerTech*, **84**, 2004, p. 74–79.

[32]   Rashidi, M.: *Development of a new generation of 12% Cr steels: Z-phase strengthened steels YR - 2015*. Department of Applied Physics, Materials Microstructure, Chalmers University of Technology, 2015.

[33]   Liu, F., Andrén, H.-O.: *Initial study on Z-phase strengthened 9-12% Cr steels by atom probe tomography*. 2010, p. 107–116.

[34]   Davidson, M.W.: http://www.microscopyu.com/articles/formulas/formulas resolution.html. *Natl. High Magn. F. Lab.*, 2016.

[35]   Goldstein, J.: *Scanning Electron Microscopy and X-ray Microanalysis*. New York: Springer US, 2003.

[36]   Kuo, W.C.H. et al.: Final Analysis: Characterisation of Catalysts Using Secondary and Backscattered Electron In-lens Detectors. *Platin. Met. Rev.*, **58** (2), 2014, p. 106–110.

[37]   Korcakova, L. et al.: Quantification of Laves phase particle size in 9CrW steel. *Mater. Charact.*, **47** (2), 2001, p. 111–117.

[38]   Dehoff, R.T., Rhines, F.N.: *Method of estimating size of discrete objects*. In: Quantitative Microscopy (Editors: R. T. DeHoff and F. N. Rhines). New York, Mcgraw-Hill, 1968, p. 75–102.

[39]   Miller, M.K., Smith, G.D.W.: *Atom Probe Microanalysis - Principles and Applications to Materials Problems*. Pittsburgh: Materials Research Society, 1989.

[40]   Mazumder, B. et al.: Reneutralization time of surface silicon ions on a field emitter. *New J. Phys.*, **12** (11), 2010, p. 113029.

[41]   Gomer, R.: *Field emission and field ionization*. Harvard University Press, 1961.

[42]   Larson, D.J. et al.: *Local Electrode Atom Probe Tomography*. New York, NY: Springer New York, 2013.

[43]   Liu, F., Andrén, H.-O.: Effects of laser pulsing on analysis of steels by atom probe tomography. *Ultramicroscopy*, **111** (6), 2011, p. 633–641.

[44]   Mamyrin, B.A. et al.: The mass-reflectron, a new nonmagnetic time-of-flight mass spectrometer with high resolution. *Sov. Phys. JETP*, **37** (1), 1973, p. 45–48.

[45]   Blavette, D. et al.: Direction et distance d'analyse à la sonde atomique. *Rev. Phys. Appliquée*, **17** (7), 1982, p. 435–440.

[46]   Bas, P. et al.: A general protocol for the reconstruction of 3D atom probe data. *Appl. Surf. Sci.*, **87-88**, 1995, p. 298–304.

[47]   Brandon, D.G.: The accurate determination of crystal orientation from field ion micrographs. *J. Sci. Instrum.*, **41** (6), 1964, p. 373–375.

[48]   Gault, B. et al.: *Atom Probe Microscopy*. New York, NY: Springer New York, 2012.

[49]   Geiser, B. et al.: Wide-Field-of-View Atom Probe Reconstruction. *Microsc. Microanal.*, **15** (S2), 2009, p. 292–293.

[50]   Gault, B. et al.: Advances in the reconstruction of atom probe tomography data. *Ultramicroscopy*, **111** (6), 2011, p. 448–457.

[51]   Cox, D.R., Hinkley, D. V: *Theoretical Statistics*. Taylor & Francis, 1979.

[52]   Dimmler, G. et al.: Quantification of the Laves phase in advanced 9–12% Cr steels using a standard SEM. *Mater. Charact.*, **51** (5), 2003, p. 341–352.

[53]   Gottstein, G.: *Physikalische Grundlagen der Materialkunde*. Berlin, Heidelberg: Springer Berlin Heidelberg, 2007.

[54]   Gale, W.F., Totemeier, T.C.: *Smithells Metals Reference Book*. Elsevier Science, 2003.

[55]   Coutsouradis, D.: *Materials for Advanced Power Engineering 1994: Proceedings of a Conference Held in Liège, Belgium, 3-6 October 1994*. Kluwer Academic, 1994.

[56]   M. K. Miller, A. Cerezo, M. G. Hetherington, and G.D.W.S.F.: *Atom Probe Field Ion Microscopy*. Clarendon Press, 1996.

[57] Isik, M.I. et al.: The nucleation of Mo-rich Laves phase particles adjacent to M23C6 micrograin boundary carbides in 12% Cr tempered martensite ferritic steels. *Acta Mater.*, **90**, 2015, p. 94–104.

[58] Aghajani, A. et al.: On the effect of long-term creep on the microstructure of a 12% chromium tempered martensite ferritic steel. *Acta Mater.*, **57** (17), 2009, p. 5093–5106.